

**Eddy phase speeds in a two-layer model of quasigeostrophic baroclinic
turbulence with applications to ocean observations**

Lei Wang* and Malte Jansen

The University of Chicago, Chicago, Illinois

Ryan Abernathey

Columbia University, New York, NY

*Corresponding author address: Lei Wang, Department of the Geophysical Sciences, University of

Chicago, 5734 S. Ellis Avenue, Chicago, IL 60637.

E-mail: leiw@uchicago.edu

ABSTRACT

10 The phase speed spectrum of ocean mesoscale eddies is fundamental to our
11 understanding of turbulent baroclinic flows. Since eddy phase propagation has
12 been shown to modulate eddy fluxes, an understanding of eddy phase speeds
13 is also of practical importance for the development of improved eddy parame-
14 terizations for coarse resolution ocean models. However, it is not totally clear
15 whether and how linear Rossby wave theory can be used to explain the phase
16 speed spectra in various weakly turbulent flow regimes. Using linear anal-
17 ysis, we identify theoretical constraints that control the eddy phase speed in
18 the two-layer quasigeostrophic (QG) model. We verify these constraints in
19 a series of nonlinear two-layer QG simulations, spanning a range of param-
20 eters with potential relevance to the ocean. In the two-layer QG model, the
21 strength of the inverse cascade exerts an important control on the eddy phase
22 speed. If the inverse cascade is weak, the phase speed spectrum is reasonably
23 well approximated by the phase speed of the linearly most unstable mode.
24 A significant inverse cascade instead leads to barotropization, which in turn
25 leads to mean phase speeds closer to those of barotropic-mode Rossby waves.
26 The two-layer QG results are qualitatively consistent with the observed eddy
27 phase speed spectra in the Antarctic Circumpolar Current and may also shed
28 light on the interpretation of phase speed spectra observed in other regions.

29 **1. Introduction**

30 Mesoscale eddies (on scales of tens to hundreds of km) are ubiquitous in the ocean, and are
31 believed to be crucial in the transport of tracers and the rectification of the mean flow (e.g., Gill
32 et al. 1974; Johnson and Bryden 1989; Hallberg and Gnanadesikan 2006; Mcwilliams 2008; Wa-
33 terman et al. 2011). Yet many of their fundamental properties are still poorly understood. This
34 contribution focuses on the question of what controls the zonal propagation (i.e. phase speed)
35 of mesoscale eddies in a two-layer model of quasigeostrophic baroclinic turbulence. Eddy phase
36 speed has recently been highlighted as an important factor in modulating the magnitude of eddy
37 fluxes (e.g. Marshall et al. 2006; Ferrari and Nikurashin 2010; Abernathey et al. 2010; Klocker
38 et al. 2012a; Klocker and Abernathey 2013; Bates et al. 2014). As described by the theory of Fer-
39 rari and Nikurashin (2010), eddy propagation relative to the background mean flow suppresses the
40 efficiency of eddy-driven mixing (see also Klocker et al. 2012a,b). Incorporating this effect into
41 mesoscale parameterizations may improve coarse-resolution ocean models which do not resolve
42 mesoscale fluxes (Bates et al. 2014). A deeper physical understanding of what controls eddy phase
43 speeds in simple models such as the one studied here is an important step towards this goal.

44 Observationally, remote sensing of sea-surface height (SSH), temperature, and color has pro-
45 vided the primary source of information about global mesoscale eddy characteristics. Several
46 different methods have been used to characterize eddy propagation speeds in these data sets. Ar-
47 guably the most straightforward method is to fit lines to a longitude-time Hovmöller diagram,
48 either by eye or using a Radon transform, as first implemented by Chelton and Schlax (1996) on
49 the 3 years of Topex/Poseidon SSH data available at the time. Wavenumber-frequency spectral
50 analysis has also been used to characterize phase speeds of SSH alone (Zang and Wunsch 1999;
51 Wunsch 2009; Wortham 2013), and of the covariance between SSH, SST and ocean color (Hill

52 et al. 2000; Cipollini et al. 1997, 2001; Killworth and Blundell 2004; Abernathey and Wortham
53 2015). Fu (2009) used space-time lag-correlation to identify the eddy propagation patterns and
54 speed. Finally, the direct tracking of individual coherent eddy features has also been implemented
55 (Chelton et al. 2011). While some of the studies cited above focus on coherent vortices, we here
56 define the eddy field to include any transient perturbation to the time-mean flow, consistent with
57 the use in the atmospheric science and general turbulence literature (well described in textbooks,
58 e.g. Pedlosky 1979; Holton 1992; McWilliams 2006). The eddy field can then be characterized by
59 the frequency-wavenumber spectrum, and eddy phase speeds are unambiguously defined by the
60 ratio of frequency to wavenumber.

61 A common feature of mesoscale turbulence is that, over most of the ocean, the observed phase
62 propagation is westward, except for the Antarctic Circumpolar Current (ACC) region and in west-
63 ern boundary current regions where Doppler shifting by the background mean flow is significant.
64 Furthermore, frequency-wavenumber analysis reveals that, at least in some regions, energy is or-
65 ganized along “non-dispersive” lines (Wunsch 2009; Early et al. 2011) (i.e. all the energy appears
66 to propagate with the same phase speed, regardless of wavenumber) - as is necessary to main-
67 tain coherent vortices (Taylor 1938; McWilliams and Flierl 1979; Nof 1981). For coherent and
68 non-dispersive eddies, the eddy phase speed is identical to the group velocity, hence theories of
69 coherent vortices may be invoked. However, it is less clear how to interpret phase speeds for
70 dispersive dynamics in the presence of instability, which is in fact not rare in the ocean.

71 Mesoscale eddies are inherently non-linear, and it is still a matter of debate to what extent their
72 properties can be understood by linear dynamics (Chelton et al. 2007; Wunsch 2009). Neverthe-
73 less, linear Rossby wave theory (well described in textbooks, e.g. Pedlosky 1979; Vallis 2006) is an
74 important starting point for understanding mesoscale eddy properties, especially in regions where
75 the flow is only weakly turbulent (Tulloch et al. 2009). It is appealing to attempt to use linear

dispersion relations to describe the nonlinear mesoscale eddy phase speeds. However, as Chelton and Schlax (1996) first noted, the standard theory for freely propagating linear baroclinic Rossby waves often underestimates the observed phase speeds. Moreover, the commonly observed non-dispersive frequency-wavenumber spectra are inconsistent with the linear Rossby wave dispersion relation. The reasons for the observed deviations from the linear Rossby wave theory became a matter of intense discussion (Killworth et al. 1997; Dewar 1998; Killworth and Blundell 2003, 2005, 2007; Tulloch et al. 2009). Klocker and Marshall (2014) recently argued that empirically eddy phase speeds over most of the ocean are reasonably well approximated by the long-wave limit of the first baroclinic mode Rossby wave phase speed, Doppler shifted by the depth averaged mean velocity \bar{U}^z . The Doppler shifting is of particular importance in the ACC region, where it explains the transition from westward to eastward phase propagation – the advection by the strong eastward mean flow here exceeds the flow-relative westward propagation speed of baroclinic Rossby waves.

This paper aims to improve our understanding of eddy phase propagation by focusing on a model of quasi-geostrophic (QG) baroclinic turbulence. The characteristics of eddy phase propagation are analyzed in a fully nonlinear model and compared to linear theory. Using the insights from QG theory, analysis of SSH observations is also presented as a comparison.

One motivation for our work is the paper by Early et al. (2011), which demonstrated the important role of nonlinearity in the formation and propagation of coherent mesoscale eddies. That study examined the evolution of a reduced-gravity QG model with and without nonlinearity. When nonlinearity was present, coherent vortices formed and the wavenumber-frequency spectrum collapsed onto a non-dispersive line, with the phase speed given approximately by the long-wave limit of the reduced-gravity mode's dispersion relation. The model used by Early et al. (2011), however, did not include baroclinicity in the background state, and cannot simulate the generation of eddies from baroclinic instability. Instead eddies were seeded using quasi-random initial conditions.

100 In a baroclinic flow, eddies and turbulence can arise as a result of baroclinic instability, and
101 the linear dispersion relation becomes more complex (literally). The relevance of neutral mode
102 baroclinic Rossby waves (which represent a true solution to the linearized equations only in the
103 absence of baroclinicity) becomes unclear in the presence of a baroclinically unstable shear flow.
104 Here we examine the eddy phase propagation properties of a homogeneous two layer QG model,
105 which is arguably the simplest possible model that can generate eddies through baroclinic insta-
106 bility. This model may be expected to reproduce some of the characteristics of eddies in the ACC
107 region and possibly the western boundary current extensions, where eddies are generated by deep-
108 mode "Phillips-like" baroclinic instability (Tulloch et al. 2011). The model instead is less likely
109 to allow for an adequate representation of the eddying flow in the subtropical regions, where we
110 do not expect such deep-mode instability (Tulloch et al. 2011).

111 This paper is structured as follows. Section 2 starts with a description of the two-layer QG model
112 and the relevant parameters. A linear stability analysis is performed to obtain the phase speeds of
113 the unstable modes, and the results are compared to the phase speeds of neutral modes obtained in
114 certain limit cases. In section 3, we conduct fully nonlinear simulations to explore the dependence
115 of the eddy phase speeds and frequency-wavenumber spectra on various model parameters; the
116 results are interpreted in terms of the linear theory discussed in section 2. We consider some
117 general properties of baroclinic turbulence, such as the barotropization in the turbulent cascade.
118 With this, we argue that, in the two-layer QG model, much of the dependence of eddy phase speeds
119 on external parameters can be understood in terms of the linear theory. In section 4 we compare
120 the results of the QG model to SSH observations. Conclusions are given in section 5.

121 **2. Linear Analysis**

122 This section describes the phase speed predictions that can be made based on linear analysis of
123 a two-layer QG model.

124 *a. The model*

125 We use a two-layer QG model on a β -plane with a flat bottom following the formulation in Flierl
126 (1978). To place the model in an oceanic regime, we consider the two layers to have a tunable
127 layer thickness ratio $\delta = H_1/H_2$, where H_1 and H_2 are the layer thicknesses for the upper layer
128 and lower layer, respectively; for the ocean, $\delta < 1$. The two-layer model is forced by an imposed
129 background vertical flow shear of $\Delta U = U_1 - U_2$ where U_i is the background zonal velocity in layer
130 i , with $i = 1$ denoting the upper layer and $i = 2$ denoting the lower layer. Q_i is the background
131 potential vorticity (PV) and q_i denotes the perturbation PV.

132 The governing equations for the PV perturbations are:

$$\begin{aligned} \frac{\partial q_1}{\partial t} + U_1 \frac{\partial q_1}{\partial x} + \frac{\partial \psi_1}{\partial x} Q_{y1} + J(\psi_1, q_1) &= ssd \\ \frac{\partial q_2}{\partial t} + U_2 \frac{\partial q_2}{\partial x} + \frac{\partial \psi_2}{\partial x} Q_{y2} + J(\psi_2, q_2) + \frac{1}{\tau_f} \nabla^2 \psi_2 &= ssd \end{aligned} \quad (1)$$

133 where the last term on the L.H.S. of the second equation denotes a linear bottom friction, with
134 a decay time scale τ_f . The Jacobian $J(\psi_i, q_i) \equiv \partial \psi_i / \partial x \partial q_i / \partial y - \partial \psi_i / \partial y \partial q_i / \partial x$ represents
135 nonlinear wave-wave interaction and ssd is small-scale dissipation, which will be ignored in the
136 linear analysis.

137 The perturbation stream functions ψ_1 and ψ_2 are related to perturbation PV through the inversion
138 relation:

$$\begin{aligned} q_1 &= \nabla^2 \psi_1 + F_1(\psi_2 - \psi_1) \\ q_2 &= \nabla^2 \psi_2 + F_2(\psi_1 - \psi_2) \end{aligned} \quad (2)$$

¹³⁹ Similarly, the background PV gradient can be related to the vertical shear and planetary vorticity
¹⁴⁰ gradient, β , via:

$$\begin{aligned} Q_{y1} &= \beta + F_1 \Delta U \\ Q_{y2} &= \beta - F_2 \Delta U \end{aligned} \quad (3)$$

¹⁴¹ where F_1 and F_2 are defined as:

$$\begin{aligned} F_1 &= \frac{1}{(\delta+1)L_d^2} \\ F_2 &= \frac{\delta}{(\delta+1)L_d^2} \end{aligned} \quad (4)$$

¹⁴² where L_d is the baroclinic deformation radius. The barotropic component of the streamfunction
¹⁴³ (ψ_{BT}) and the baroclinic component of the streamfunction (ψ_{BC}) can be defined (Flierl 1978; Arbic
¹⁴⁴ and Flierl 2004) as:

$$\begin{aligned} \psi_{BT} &= \frac{1}{1+\delta} (\delta \psi_1 + \psi_2) \\ \psi_{BC} &= \frac{\sqrt{\delta}}{1+\delta} (\psi_1 - \psi_2) \end{aligned} \quad (5)$$

¹⁴⁵ In this study, we assume a positive vertical mean flow shear (i.e. eastward), which is consistent
¹⁴⁶ with observations over most eddy-rich regions of the world oceans.

¹⁴⁷ For instability to occur, in the absence of friction, the PV gradient must change sign between
¹⁴⁸ the upper layer and lower layer, so as to support counter-propagating Rossby waves. Q_{y1} is always
¹⁴⁹ larger than zero for a positive vertical mean flow shear, and thus stability is governed by the non-
¹⁵⁰ dimensional criticality parameter:

$$\xi = \frac{F_2 \Delta U}{\beta}. \quad (6)$$

¹⁵¹ If $\xi > 1$ (equivalent to $Q_{y2} < 0$), instability can occur in the inviscid limit.

¹⁵² More generally, in the presence of friction, we can define three independent non-dimensional
¹⁵³ parameters. Normalizing length scales with L_d and time scales with $L_d/\Delta U$, we obtain:

¹⁵⁴ 1. layer thickness ratio δ

155 2. non-dimensional bottom frictional damping rate $\tau_f^{*-1} = L_d / (\Delta U \tau_f)$

156 3. non-dimensional planetary vorticity gradient $\beta^* = \beta L_d^2 / \Delta U$.

157 The non-dimensional planetary vorticity gradient is related to the criticality parameter via:

$$\xi = \frac{\delta}{(1 + \delta)\beta^*}. \quad (7)$$

158 These three parameters collectively determine the basic properties of the two-layer QG model. We
159 explore different flow regimes by varying these three parameters.

160 *b. Linear dispersion relations*

161 In a square, doubly periodic domain, we assume a plane-wave solution:

$$\psi_i = \Re \tilde{\psi}_i e^{i(kx+ly-\omega t)} = \Re \tilde{\psi}_i e^{ik(x-ct)+ily} \quad (8)$$

162 where k and l are the zonal and meridional wavenumbers, and \Re denotes the real part. Generally
163 $c \equiv \omega/k$ is a complex number whose real part represents the zonal phase propagation speed and
164 imaginary part represents the growth/decay rate of an unstable mode. Linear solutions are obtained
165 by replacing terms in the linearized equation (1) with this plane-wave solution.

166 Before considering the full linear instability problem, we first review the three neutral mode
167 solutions which arise in relevant limit cases. When the lower layer is either much deeper than
168 the upper layer, or when bottom friction is very strong, the lower layer flow becomes very weak,
169 i.e. $\psi_2 \ll \psi_1$. The lower layer equation in (1) then becomes a second-order equation, while the
170 linearized upper-layer equation to first order yields the reduced gravity model (considered by Early
171 et al. 2011):

$$\frac{\partial}{\partial t}(\nabla^2 \psi_1 - F_1 \psi_1) + U_1 \frac{\partial}{\partial x}(\nabla^2 \psi_1 - F_1 \psi_1) + \frac{\partial \psi_1}{\partial x} Q_{y1} = 0. \quad (9)$$

¹⁷² The dispersion relation for the reduced gravity mode is

$$c_{RG} = \frac{\omega}{k} = U_1 - \frac{Q_{y1}}{k^2 + l^2 + F_1} \quad (10)$$

¹⁷³ where the subscript *RG* means “reduced-gravity”.

¹⁷⁴ On the other hand, in the limit of vanishing vertical shear ($\Delta U \rightarrow 0$) and neglecting bottom
¹⁷⁵ friction, the eigenvalue problem posed by the linearized version of equation (1) yields two neutral
¹⁷⁶ modes: a barotropic mode and a baroclinic mode. The dispersion relation for the barotropic mode
¹⁷⁷ is:

$$c_{BT} = U_b - \frac{\beta}{k^2 + l^2} \quad (11)$$

¹⁷⁸ where $U_b \equiv (\delta U_1 + U_2)/(1 + \delta)$ is the barotropic mean flow¹.

¹⁷⁹ The dispersion relation for the baroclinic mode is:

$$c_{BC} = U_b - \frac{\beta}{k^2 + l^2 + 1/L_d^2} \quad (12)$$

¹⁸⁰ where L_d is the deformation radius of the first baroclinic mode. The long-wave limit of the baro-
¹⁸¹ clinic mode ($c_{BC} \approx U_b - \beta L_d^2$) has recently been argued to provide a good fit to the eddy phase
¹⁸² propagation characteristics obtained from altimetric observations. (Tulloch et al. 2009; Klocker
¹⁸³ and Abernathey 2013; Klocker and Marshall 2014; Abernathey and Wortham 2015)

¹⁸⁴ Comparing c_{BC} with c_{RG} , three major differences appear: (1) c_{BC} is Doppler shifted by the
¹⁸⁵ depth-average flow, while c_{RG} is Doppler shifted by the upper layer flow. (2) c_{BC} feels the plane-
¹⁸⁶ tary vorticity gradient β , while c_{RG} feels the upper layer PV gradient Q_{y1} . (3) c_{BC} feels the first
¹⁸⁷ baroclinic deformation radius, while c_{RG} feels the “upper layer deformation radius”, $1/\sqrt{F_1}$. In the
¹⁸⁸ long-wave limit, the reduced gravity mode dispersion relationship simplifies due to a cancellation

¹Formally the solutions in Eqs. (11) and (12) are derived assuming $\Delta U = 0$ and thus $U_b = U_1 = U_2$. There is thus some arbitrariness in the formulation of the “Doppler shift” in Eqs. (11) and (12). The formulations here were chosen such that the phase speeds remain independent of any background baroclinicity that may be present.

189 between the effects of the upper layer flow on the Doppler shift and on the PV gradient, which
 190 yields $C_{RG} = -\beta/F_1 + U_2$. In this limit the reduced gravity dispersion relationship resembles that
 191 for the baroclinic mode, but with the difference that the apparent Doppler shift is given by the
 192 lower layer flow speed, and the relevant deformation radius is that of the upper layer.

193 *c. Linear instability*

194 This subsection revisits the instability properties of the full two-layer QG model. Linearizing
 195 Eq. (1) and using (2) and (8) yields:

$$\begin{pmatrix} -(U_1 - c)(k^2 + l^2 + F_1) + Q_{y1} & (U_1 - c)F_1 \\ (U_2 - c)F_2 & -(U_2 - c)(k^2 + l^2 + F_2) + Q_{y2} + \frac{i}{k\tau_f}(k^2 + l^2) \end{pmatrix} \begin{pmatrix} \psi_1 \\ \psi_2 \end{pmatrix} = 0 \quad (13)$$

196 For non-trivial solutions, the determinant of coefficients must be zero. This provides a quadratic
 197 equation for c , which yields two solutions. In the absence of bottom friction, a pair of complex
 198 conjugate solutions are obtained for baroclinically unstable mean shears ($\xi > 0$), denoting one
 199 growing and one decaying mode.

200 We now review the impact of nonzero friction on the linear stability analysis, which affects
 201 both growth rates and phase speeds. Numerical solutions for the growth rate and phase speeds
 202 are computed using parameters roughly characteristic of the ACC: $\delta = 0.25$, $\Delta U = 0.04 \text{ m/s}$ and
 203 $L_d = 15 \text{ km}$. The layer depth ratio of 0.25 is roughly consistent with the depth of the sign-reversal
 204 in the observed extra-tropical zonal-mean QGPV gradient (Tulloch et al. 2011). Similarly, the
 205 vertical shear and deformation radius are in rough agreement with observations in the ACC region.
 206 We will return to a more quantitative comparison between the QG model and the observations in
 207 section 4. The meridional wavenumber l is set to zero to obtain the fastest growing modes (e.g.

208 Vallis 2006). The role of non-zero meridional wavenumber l will be discussed in the following
209 sections.

210 The upper panel of Fig. 1, shows the linear growth rates as a function of wavenumber for
211 different values of bottom friction. When friction is absent, both a short-wave cutoff and long-
212 wave cutoff can be identified. However, with increasing frictional strength, the short waves and
213 some long waves are destabilized while maximum growth rates decrease, as first discussed by
214 Holopainen (1961). The length scale of the most unstable modes also slightly decreases with
215 increasing frictional strength. The lower panel in Fig. 1 shows the corresponding phase speeds.
216 Unstable modes propagate eastward ($\Re(c) > 0$) at most wavelengths. Only when friction is weak,
217 the phase speed can be slightly westward ($\Re(c) < 0$).

218 The dispersion curves for the reduced gravity mode (dashed) and the barotropic mode (dot-
219 dashed) are also plotted in the lower panel of Fig. 1. The phase speeds of the linearly unstable
220 modes consistently fall between these two neutral curves. Since c_{RG} represents the limit case
221 where the lower layer is at rest, it is perhaps not surprising that the phase speeds of the unsta-
222 ble modes approach c_{RG} as bottom friction is increased. In fact, it appears that (10) is a useful
223 approximation to the phase speed of the unstable modes in a realistic parameter regime.

224 The baroclinic dispersion curve c_{BC} is also plotted in the lower panel of Fig. 1 for comparison.
225 The baroclinic mode phase speed shows a relatively weak wavenumber dependence and is less
226 clearly related to the full linear instability problem, although the overall phase speed is close to
227 that of the fastest growing modes. Whether the agreement between the baroclinic mode phase
228 speed and the phase speed of the fastest growing mode is a coincidence or is driven by some
229 physical mechanism remains unclear.

230 Notice that c_{BC} and c_{RG} are not always easy to distinguish in the real ocean. For example, in
231 the sub-tropical gyres, the first baroclinic mode typically becomes strongly surface intensified –

corresponding to an upper layer that is much shallower than the lower layer. The upper layer deformation radius in c_{RG} then is well approximated by the first baroclinic deformation radius as in c_{BC} . Moreover, the vertical shear is typically weak, such that the upper-ocean PV gradient in c_{RG} approximately reduces to the planetary vorticity gradient as in c_{BC} , and Doppler shifting by the barotropic flow becomes indistinguishable from Doppler shifting by the upper-ocean flow. On the other hand, in other regions, such as the ACC, the differences between c_{BC} and c_{RG} should be more pronounced.

3. Nonlinear Model

The linear analysis described above reveals the phase speeds of linear modes. However, in a nonlinear equilibrated state, it is not *a priori* clear which wavenumbers get energized and whether the eddies in the nonlinear flow actually follow a linear dispersion relation. This section presents frequency-wavenumber spectra and phase speed spectra from a series of nonlinear two-layer QG simulations and compares them to the predictions from linear theory.

a. Model description and methods

We numerically solve the fully nonlinear two-layer QG model described by equation (1) using the open-source python package pyqg (Abernathay et al. 2015). We use a doubly periodic domain with a horizontal resolution of 256×256 grid points in real space. Enstrophy is removed near the grid scale with an exponential filter which is identical to that described in Arbic and Flierl (2004).

The parameters in the control simulation are as in the linear analysis discussed in section 2:

$$L_d = 15 \text{ km} , \quad U_1 = 0.04 \text{ m/s} , \quad U_2 = 0 \text{ m/s} , \quad \tau_f = 20 \text{ days} , \quad \delta = 0.25 . \quad (14)$$

The frictional decay rate of $(20 \text{ days})^{-1}$ is empirically chosen to obtain eddy properties that are roughly consistent with observations in the ACC region. Determination of a realistic frictional

time scale from first principles is not straightforward, as it crudely represents various routes to dissipation near the bottom boundary (see also Arbic and Flierl 2004). The positive mean flow vertical shear of 0.04 m/s is consistent with observations in the ACC region. The parameters in our two-layer QG model correspond to a non-dimensional criticality parameter of $\xi \approx 2.37$, which is moderately supercritical.

As case studies, we present three reference simulations. These three simulations use the above listed parameters but with different frictional strengths. In addition to the control run which uses $\tau_f = 20 \text{ days}$, the strong friction run and the weak friction run use $\tau_f = 10 \text{ days}$ and $\tau_f = 40 \text{ days}$, respectively. In Fig. 2, the Hovmöller diagram of the upper layer streamfunction in the control run suggests no clear preferential direction of propagation. Comparing all three simulations in Fig. 2 suggests that decreasing the frictional strength to $(40 \text{ days})^{-1}$ enhances westward propagation; while increasing the frictional strength to $(10 \text{ days})^{-1}$ favors eastward propagation.

To comprehensively examine the phase speeds in the two-layer QG model, in addition to the three reference simulations, we conduct several groups of experiments, each varying only one non-dimensional parameter. Each group includes more than 20 simulations to explore the effect of variations in the non-dimensional parameters over at least one order of magnitude.

1. In the experiments dubbed THIC, the layer thickness ratio δ is varied, while τ_f^* and β^* are held fixed.

2. In the FRIC experiments, τ_f^* is varied, while δ and β^* are held fixed.

3. In the BETA experiments, β^* is varied, while δ and τ_f^* are held fixed. The additional group BETA-hf is similar to the BETA experiments, but with strong frictional strength.

274 The parameters considered here do not give rise to regimes with strong jets (Rhines 1975; Maltrud
275 and Vallis 1991). Among all simulations, the output data of the first 10 years is dropped, and
276 streamfunction snapshots for both layers from the following 50 years are sampled every 5 days.

277 Analysis of the nonlinear simulations is based on spectral analysis in wavenumber and frequency
278 space (Hayashi 1971). The streamfunction $\psi_i(x, y, t)$ is Fourier-transformed into spectral space as
279 $\hat{\psi}_i(k, l, \omega)$, where k , l , and ω are zonal wavenumber, meridional wavenumber, and frequency,
280 respectively. By multiplication of the three-dimensional streamfunction variance spectrum with
281 the total wavenumber and integration over all frequencies ω , the total EKE as a function of zonal
282 and meridional wavenumber can be obtained:

$$E_i(k, l) = \int \frac{1}{2}(k^2 + l^2) |\hat{\psi}_i(k, l, \omega)|^2 d\omega \quad (15)$$

283 Fig. 3 shows the upper-layer total eddy kinetic energy as a function of zonal and meridional
284 wavenumber, $E_1(k, l)$, for our three reference simulations. The total EKE is nearly isotropic for all
285 three reference simulations. Because of the isotropic behavior in our model, and the focus on zonal
286 phase propagation, we emphasize the dependence of EKE on frequency and zonal wavenumber
287 k . Rather than showing total EKE, we moreover focus on meridional velocity variance spectra
288 (hereafter “transverse spectra”), which can be obtained by integrating the streamfunction variance
289 spectrum over all zonal wavenumbers and multiplying by k^2 :

$$E_{\perp i}(k, \omega) = k^2 \int \frac{1}{2} |\hat{\psi}_i(k, l, \omega)|^2 dl \quad (16)$$

290 The advantages of using transverse energy spectra are discussed in the appendix.

291 *b. General Results*

292 In this section, we discuss the general characteristics of the turbulent flow fields in the fully
293 nonlinear two-layer QG simulations, and explore the dependence of the eddy properties on the

three non-dimensional parameters. Linear theory highlights the different propagation behavior of the barotropic and baroclinic modes, so this decomposition is a useful starting point for our analysis of the nonlinear simulations. Using equation (5), we can separate the energy spectra into barotropic and baroclinic components. In Fig. 4, solid curves show the ratio of barotropic mode EKE to total EKE as a function of zonal wavenumber. This ratio is bigger toward small wavenumbers in the control experiment, indicating a trend towards enhanced barotropitization at larger scales. Comparing all three reference simulations, the barotropitization is enhanced when friction is weak, and vice versa. This barotropitization can partially be attributed to an increasing barotropic contribution to the linearly most unstable modes. However, linear theory alone does not fully predict the strong barotropitization observed at low wavenumbers. The strong barotropitization is instead likely attributable to nonlinearity.

In Fig. 5, we show the parameter dependence of the ratio of barotropic EKE to total EKE by averaging over all horizontal wavenumbers and frequencies, in all simulations in THIC, FRIC, BETA and BETA-hf. The flow becomes more barotropic when (1) layer thickness ratio approaches unity, (2) friction is reduced, (3) β^* is reduced. All of these dependencies are in qualitative agreement with previous results (e.g. Arbic and Flierl 2004). Throughout most of the parameter range, ratios of barotropic EKE and total EKE in nonlinear simulations are larger than the corresponding ratios predicted by linear instability analysis, suggesting an important role of nonlinearity. In the simulations whose total EKE is dominated by the barotropic mode, we expect the dispersion relation of the barotropic mode to provide a better prediction of the eddy phase speeds. We will test this hypothesis in the next subsection.

In addition to barotropitization, non-linear eddy-eddy interactions tend to lead to an increase in the horizontal eddy scale, beyond the scale of the most unstable mode. To characterize length scales, we integrate the power spectra over all frequencies to obtain a univariate zonal wavenumber

318 spectrum for each experiment. Furthermore, the spectral energy budget at the zonal wavenumber
319 k can be written as below, following the formalisms in Jansen and Held (2014):

$$\partial_t E_k = S_k + TA_k + TK_k - F_k - V_k \quad (17)$$

320 Here, E_k , S_k , TA_k , TK_k , F_k , and V_k represent total kinetic energy for both layers, the extraction
321 of available potential energy (APE) from the prescribed background state, spectral transfer of
322 APE, spectral transfer of kinetic energy, frictional dissipation by bottom drag, and small scale
323 dissipation, respectively.

324 The sum of S_k and TA_k can be interpreted as the conversion from available potential energy to
325 eddy kinetic energy. S_k and TA_k can be calculated through

$$\begin{aligned} S_k &= \frac{U}{L_d^2} \Re[ik \widehat{\psi_{BT}} \widehat{\psi_{BC}}^*]_k \\ TA_k &= -\frac{1}{L_d^2} \Re[\widehat{\psi_{BC}}^* J(\widehat{\psi_{BT}}, \widehat{\psi_{BC}})]_k \end{aligned} \quad (18)$$

326 where the asterisk denotes the complex conjugate, and $\widehat{(..)}$ denotes the Fourier transform, here
327 with respect to zonal wavenumber.

328 In Fig. 6, we use the diagnosed spectra of net conversion from APE to EKE (top row) to indicate
329 the scale at which kinetic energy is injected into the system. The peak in the conversion spectrum
330 roughly coincides with the peak in the linear growth rate, which is shown in the bottom row.
331 The departure between the peak in the conversion spectrum and the peak in the barotropic EKE
332 spectrum gives an indication of the inverse cascade range.

333 The THIC experiments (first column) show that simulations with equal layer depths exhibit a
334 slightly enhanced inverse cascade compared with simulations with a shallower upper layer. The
335 FRIC experiments (second column) exhibit the most significant changes in the inverse cascade
336 range, with a strong inverse cascade found in limit of weak friction, consistent with Arbic and
337 Flierl (2004). There is no direct correspondence between the most unstable wavenumbers and

338 the energy containing wavenumbers, and linear stability analysis only predicts the injection scale.
339 While the large inverse cascade in the limit of weak friction is the result of strong nonlinear eddy-
340 eddy interactions, we note that the largest eddies are near the wave-turbulence crossover (Rhines
341 1979), suggesting that linear dynamics are likely to remain relevant. The BETA and BETA-hf
342 experiments show that the energy cascade range is reduced for large β^* , which is in agreement
343 with the general understanding that the beta-effect limits the inverse energy cascade (Rhines 1979).
344 However, for small β^* the halting scale converges to a constant value, which again depends on the
345 bottom friction (compare the third and fourth columns in Fig. 6).

346 In summary, although all non-dimensional parameters influence the strength of the inverse cas-
347 cade, it is here found to be most sensitive to the frictional strength. Many theoretical arguments
348 have been developed to predict the halting scale of the inverse energy cascade (e.g. Rhines 1979;
349 Held and Larichev 1996; Arbic and Flierl 2004; Thompson and Young 2007; Jansen et al. 2015),
350 and the results obtained here appear to be broadly consistent with this previous work. However,
351 our focus is on the eddy phase speed, and a detailed comparison between inverse cascade strength
352 and different scaling laws is beyond the scope of this contribution.

353 *c. Phase Speed Spectra*

354 1) CASE STUDIES

355 To characterize zonal phase speeds in the nonlinear simulations, we now consider the
356 wavenumber-frequency spectrum, which can be compared to the linear dispersion relationships
357 discussed in section 2. To further quantify the dominant phase speed, the wavenumber-frequency
358 spectrum can be transformed to a wavenumber-phase-speed spectrum, following Randel and Held
359 (1991) (see also Abernathey and Wortham 2015). For easy comparison to observations, which are
360 available only for the near-surface flow, all analysis of wavenumber-frequency spectra is presented

for the upper model layer. The top row in Fig. 7 shows the wavenumber-frequency transverse EKE (E_{\perp}) spectra for our three reference cases: the control run, weak friction run, and strong friction run. Since E_{\perp} is proportional to k^2 times the stream-function variance (Eq. 16), the E_{\perp} spectra by construction vanish in the limit of vanishing zonal wavenumber and highlight the wavenumber range of the energy-containing eddies. To make a connection between E_{\perp} spectra and the streamfunction spectra often considered in the oceanographic literature (e.g. Wunsch 2009), and to investigate the dispersion relation at all zonal wavenumbers, the middle row of Fig. 7 shows the wavenumber-frequency spectra normalized by the total power at each zonal wavenumber. Finally, the bottom row shows the interpolated wavenumber-phase-speed spectra of E_{\perp} (without any normalization).

To facilitate the comparison with linear theory, the linear dispersion relations discussed in Sec. 2 are also plotted in Fig. 7. We adopt spectral moments to characterize the length scales of the turbulence, as in numerous prior studies (e.g. Rhines 1975; Scott and Wang 2005; Tulloch et al. 2011; Abernathey and Wortham 2015). To quantitatively examine the accuracy of linear predictions, at each zonal wavenumber, we compare the diagnosed mean eddy phase speeds, $\tilde{C}_O(k)$, with the predicted mean eddy phase speeds according to the different linear dispersion relationships, $\tilde{C}_X(k)$. The diagnosed mean eddy phase speed $\tilde{C}_O(k)$ is defined as the first moment of the wavenumber-phase speed spectrum $E_{\perp}(k, c)$:

$$\tilde{C}_O(k) = \frac{\int E_{\perp}(k, c) \cdot c dc}{\int E_{\perp}(k, c) dc}. \quad (19)$$

The predicted mean eddy phase speed for a given mode is computed as

$$\tilde{C}_X(k) = \frac{\int E_{\perp}(k, l) \cdot C_X(k, l) dl}{\int E_{\perp}(k, l) dl}, \quad (20)$$

where $C_X(k, l)$ is given by the linear dispersion relation of the respective mode, i.e. $C_{BT}(k, l)$, or $C_{RG}(k, l)$, or $C_{BC}(k, l)$. Eq. (20) can be used to infer an effective meridional wavenumber, l_{eff} ,

such that $\tilde{C}_X(k) = C_X(k, l_{eff})$, which mostly lies in between $l = 0$ and $l = k$, but varies significantly with k (Fig. 7). The varying effective meridional wavenumber is not a sign of anisotropy, but simply the result of projecting the two-dimensional EKE spectrum on zonal wavenumber (see appendix). Observed and predicted mean frequencies are computed as $\tilde{\omega}_O(k) = \tilde{C}_O(k)k$ and $\tilde{\omega}_X(k) = \tilde{C}_X(k)k$.

Focussing first on the normalized frequency-wavenumber spectrum of the control experiment (middle panel of the middle row of Fig. 7), the barotropic dispersion curve $\tilde{\omega}_{BT}$ and the reduced-gravity curve $\tilde{\omega}_{RG}$ overlap with different energy-containing regions of the power spectrum— $\tilde{\omega}_{BT}$ agrees better with the low-frequency part the spectrum, whereas $\tilde{\omega}_{RG}$ traces the high-frequency, high-wavenumber end of the spectrum. In comparing the three simulations, as frictional strength varies from strong to weak, the maximum of the raw frequency-wavenumber E_\perp spectrum (top row of Fig. 7) shifts from positive frequency toward negative frequency. Correspondingly, in the phase speed spectra (bottom row of Fig. 7) the predominant phase speed shifts from eastward to westward when friction is varied from strong to weak values. The peak of the energy spectrum generally falls roughly within the region enclosed by the two neutral dispersion curves $\tilde{\omega}_{BT}$ and $\tilde{\omega}_{RG}$. The phase speed of the baroclinic mode in its long-wave limit (proposed as a predictor of eddy phase speeds by Klocker and Marshall (2014)) agrees reasonably well with the energy peak in the control run and the strong friction run, but does not capture the fast westward propagation at weak friction. The faster westward propagation at weak friction is qualitatively consistent with the increased inverse energy cascade (Fig. 6) and barotropization (Fig. 5).

To quantify the overall accuracy of a particular linear model in a simulation, a normalized root-mean-square error (RMSE) for the phase speed is defined as:

$$\Delta\tilde{C}_X = \left[\frac{\int_0^{k_{max}} (\tilde{C}_X(k) - \tilde{C}_O(k))^2 E_\perp(k) dk}{\int_0^{k_{max}} \tilde{C}_O(k)^2 E_\perp(k) dk} \right]^{\frac{1}{2}}, \quad (21)$$

404 where k_{max} is a cutoff wavenumber, chosen to reduce the numerical bias due to limited sampling
 405 rates of the model output – higher wavenumbers tend to be associated with higher frequencies,
 406 which in turn require higher sampling rates. Based on our model parameter range and output
 407 sampling rate, k_{max} is chosen as 0.01 cpkm. This range contains about 80 - 90 % of the total
 408 transverse EKE. The values of $\Delta\tilde{C}_X$ for the different linear models are given on the bottom panels
 409 of Fig. 7. Consistent with the visual impression, in the strong friction case, the reduced-gravity
 410 mode has the smallest normalized RMSE, while in the weak friction case, the barotropic mode has
 411 the smallest normalized RMSE.

412 2) PARAMETER SPACE INVESTIGATION

413 To examine how phase speeds vary in the THIC, FRIC, BETA and BETA-hf experiments, for
 414 each experiment, we calculate a diagnosed mean phase speed following:

$$\tilde{C}_O = \frac{\iint E_{\perp}(k, c) \cdot c dcdk}{\iint E_{\perp}(k, c) dcdk}. \quad (22)$$

415 Notice that Eq. (22) differs from Eq. (19) by an additional integration over all zonal wavenumbers,
 416 thus yielding a single characteristic mean phase speed for each simulation.

417 Correspondingly, for each experiment, we calculate a predicted mean phase speed \tilde{C}_X following:

$$\tilde{C}_X = \frac{\iint E_{\perp}(k, l) \cdot C_X(k, l) dkdl}{\iint E_{\perp}(k, l) dkdl}. \quad (23)$$

418 In Fig. 8, the top row compares diagnosed and predicted phase speeds (plotted on top of the power
 419 spectra), while the bottom row shows the growth rate as a function of phase speed from the linear
 420 stability analysis. For easy comparison, the general structure of Fig. 8 is similar to that of Fig. 6.

421 We first focus on the effect of varying layer thickness ratio in the THIC experiments (left col-
 422 umn of Fig. 8). For shallow upper layer (small δ), the EKE-containing eddies propagate eastward,
 423 which is close to the linear prediction from baroclinic instability analysis (bottom row). For rela-

tively shallow upper layer, the mean phase speed is also reasonably well captured by the predicted reduced-gravity curve \tilde{C}_{RG} . In the equal layer depth limit ($\delta \approx 1$), the observed mean phase speed is better captured by the barotropic mode predictor, \tilde{C}_{BT} . We also see an increase in the spread of the phase speed spectrum with increased layer depth ratio, which is indicative of increased turbulence leading to the dominance of chaotic advection.

We next focus on the role of varying the non-dimensional planetary vorticity gradient in the BETA and BETA-hf experiments (right two columns of Fig. 8). For strong non-dimensional beta (marginal criticality), the most energetic eddies generally propagate eastward, consistent with the eastward propagation of the linearly most unstable modes. As β^* is reduced (criticality increases), the mean eddy phase speed in BETA shifts slightly westward and then slightly back eastward, while the mean eddy phase speed in BETA-hf shifts very slightly eastward across the entire parameter space. In the BETA experiments, as β^* is reduced, there appear to exist two parameter regimes: First, reducing the non-dimensional beta leads to barotropization, which leads to more westward phase propagation as the mean phase speed moves towards the phase speed of the barotropic mode. As β^* is further reduced, the barotropic mode phase speed itself becomes weaker and eventually turns eastward. In the BETA-hf experiments, on the other hand, friction suppresses barotropization and the mean phase speed remains well approximated by the reduced gravity mode through the entire range of β^* . In both the BETA and (to a lesser degree) BETA-hf experiments, we also see an increase in the spread of the phase speed spectrum with decreasing β^* . This is consistent with theoretical predictions, as the more supercritical mean state is expected to lead to more vigorous turbulence (e.g. Held and Larichev 1996).

By and large, varying the layer thickness ratio and non-dimensional beta does not change the mean phase speed substantially. However, in the FRIC experiments (second column in Fig. 8), when friction becomes weaker, the predominant phase speed shifts significantly from eastward

propagation to fast westward propagation. In the strong friction regime, the mean phase speed is well captured by the predicted phase speed for the reduced gravity mode. In the weak friction regime, on the other hand, the mean phase speed is well captured by the phase speed of the barotropic neutral mode, and is far away from the predictions of linear stability analysis (compare to the second row). As shown in Fig. 6 and Fig. 5, the weak friction regime is characterized by a robust inverse energy cascade and barotropization, indicating that non-linear eddy-eddy interactions are the main reason for the departure of the eddy phase speeds from linear stability predictions. In spite of the strong nonlinearity in the weak friction limit, the linear barotropic-mode dispersion relation provides a good predictor for the eddy phase speeds, given the energy containing wavenumber. The baroclinic and barotropic modes were also analyzed separately (not shown) and were found to have similar spectra, indicating tight coupling between modes.

The normalized RMSE in Fig. 9 confirms the aforementioned descriptions by quantifying the skill of the respective theoretical dispersion relations throughout the entire parameter space. In the THIC and FRIC experiments, the barotropic mode provides the most accurate prediction in one limit, whereas the reduced-gravity mode provide the most accurate prediction in the other limit. In the BETA and BETA-hf series, the reduced-gravity mode provides the best predictor throughout the parameter range,

We conclude that in the two-layer model, the strength of the inverse cascade determines the eddy length scale and amount of barotropization, which in turn determines the predominant eddy phase speed. When the flow is largely concentrated in the upper-layer (e.g. due to strong bottom friction), the reduced-gravity dispersion curve c_{RG} is more apt, whereas when the flow is largely barotropic, the barotropic dispersion curve c_{BT} gives a better estimate. The baroclinic mode dispersion relation was generally found to be a less useful predictor than the reduced gravity mode.

471 **4. Comparison to Observations**

472 In this section, we explore spatial-temporal spectral analysis of satellite observations and com-
473 pare them to the QG model results discussed in the previous sections. The point of this exercise is
474 to test the correspondence between the physical arguments in a two-layer QG model given above
475 and the observed eddy propagation in a qualitative way. Our main testbed is a selected region
476 of the Antarctic Circumpolar Current (ACC) in the Southern Ocean, which is largely zonally-
477 symmetric and shares some essential properties with the two-layer QG model. As a comparison,
478 we also revisit a subtropical region considered in Wunsch (2009), which is characterized by more
479 “non-dispersive” eddies and a shallow-mode instability that is not well represented by a zonally-
480 symmetric two-layer QG model (Tulloch et al. 2009).

481 *a. Data*

482 We use 22 years of gridded geostrophic velocity anomalies and absolute geostrophic velocities
483 produced by the SSALTO/DUACS multission altimeter processing system and distributed by
484 AVISO. Since the focus of this study is on the extra-tropical region, where the assumption of
485 geostrophy is largely valid, we expect the AVISO products to reasonably reflect the underlying
486 flow field. The grid size of AVISO is 0.25° , which in the ACC region corresponds to around 15
487 km. Low-pass Lanczos filtering has been applied to the product during the gridding procedure to
488 remove the residual noise and small scale signals below 65 km globally. Since in this study we
489 focus on mesoscale eddies, which typically are larger than 200 km (Stammer 1997), the 65 km
490 cutoff scale of the filter should not bias our core results, though some caution must be used in the
491 interpretation of the data at higher wavenumbers.

492 For comparison with the two-layer QG model, the ideal testbed in observations should have a
493 homogeneous zonal background flow and relatively small topographic effect on the eddies. We

choose two regions with relatively flat topography and homogeneous background flow in a subtropical region and the ACC, respectively. Both regions are big enough compared to its eddy scales. The subtropical region is in the northeast Pacific between 22°N and 32°N, and from 180°W to 140°W, centered around the cross section discussed in Wunsch (2009) (hereafter W09 Box). The region from the ACC is between 54°S and 64°S in the southeast Pacific from 117.375°W to 77.375°W (hereafter ACC Box). Fig. 10 shows the climatological zonal component of the absolute geostrophic velocities for the two chosen regions, averaged for the year 2012. Both these regions are characterized by roughly zonally homogeneous mean flow. The ACC Box region is at the core of the ACC and has a climatological zonal surface mean flow much stronger than the zonal surface mean flow in the W09 Box region. Though both regions appear to be predominantly zonally symmetric, we note that even a small zonal variation of the basic state can have significant impacts on the instability problem (Tulloch et al. 2009). This may be of importance in particular for the W09 region, where the zonal mean shear alone is stable to deep-mode baroclinic instability.

507 *b. Methods*

To compare the observations with the results inferred from the two-layer QG model, we need to match the observed mean flow and stratification profiles to the relevant parameters in the QG model. A recipe for this procedure was developed by Flierl (1978) based on a vertical mode decomposition. If the flow in the continuously stratified fluid is dominated by the barotropic and first baroclinic mode, we can construct an analog two-layer model which adequately reproduces the dynamics of these two modes.

The first-baroclinic-mode structure of the continuously stratified QG equations provides a constraint for the baroclinic deformation radius and layer thickness ratio in the two-layer QG analogue. Following Flierl (1978), we compute the layer thickness ratio to match the baroclinic

517 self-interaction:

$$\delta = \frac{1}{4} [\sqrt{\xi_{111}^2 + 4} - \xi_{111}]^2, \quad (24)$$

518 where the nonlinear baroclinic self-interaction, ξ_{111} , is determined based on the first baroclinic
519 mode structure, $\Phi_1(z)$, as $\xi_{111} = 1/H \int_{-H}^0 \Phi_1^3(z) dz$.

520 Following Tulloch et al. (2009), based on the vertical buoyancy profile, $N(z)^2$, we calculate the
521 first eigenmode structures, $\Phi_i(z)$, (right panel in Fig. 11) and eigenvalues, $K_d = 1/L_d$, from the
522 Sturm-Liouville equation:

$$\frac{d}{dz} \left(\frac{f^2}{N^2(z)} \frac{d\Phi}{dz} \right) = -K_d^2 \Phi, \quad (25)$$

523 where the buoyancy-frequency profile $N^2(z)$ is estimated from the neutral density data in Gouretski
524 and Koltermann (2004) at the two chosen regions (left panel in Fig. 11). The right panel of Fig. 11
525 shows the first baroclinic mode in the two regions. In the ACC Box, it has a deep structure, and a
526 deformation radius of 14 km. The equivalent layer thickness ratio is found to be $\delta \approx 0.49$. On the
527 other hand, the first baroclinic mode in the W09 Box is more surface-intensified, with a radius of
528 deformation of 43 km and an equivalent layer thickness ratio $\delta \approx 0.23$.

529 Fig. 11 shows the vertical structure of the climatological zonal-mean zonal current in the W09
530 and ACC Boxes. The mean flow for the W09 Box is taken from the ECCO state estimate (Wunsch
531 and Heimbach 2007), while the mean flow in the ACC Box is taken from the Southern Ocean
532 State Estimate (Mazloff et al. 2010). In the ACC Box, almost all zonal mean KE projects onto
533 the barotropic mode and first baroclinic mode (blue and black curves in Fig. 11). This projection
534 corresponds to a vertical mean flow shear of 2.8 cm/s in the two-layer QG analogue, on the same
535 order as the vertical mean flow shear considered in our QG two-layer reference setup in section 2
536 and 3. Therefore the baroclinic instability in the ACC Box is expected to be dominated by deep
537 “Phillips-type” instabilities, consistent with the findings of Tulloch et al. (2011).

538 In the W09 Box, the projection on the two-layer QG model gives a mean state with a vertical
539 mean flow shear of 0.22 cm/s, sub-critical to a zonally-symmetric two-layer QG-type baroclinic
540 instability in the absence of friction. This points to several alternative routes through which eddies
541 in this regions are generated: (1) a non-zero meridional shear; (2) instabilities of higher vertical
542 modes; (3) generated non-locally. Even though a zonally-symmetric two-layer QG model in this
543 region is insufficient to directly generate baroclinic eddies, it might still be relevant to interpret
544 the local behavior of eddies that may have been generated through other processes (so long as the
545 surface EKE is dominated by the barotropic and first baroclinic mode). In particular the neutral
546 reduced-gravity mode may be relevant for predicting eddy phase speeds in regions with strongly
547 surface intensified stratification and weak vertical shear, such as the W09 region (e.g. Early et al.
548 2011).

549 *c. Phase speed spectra*

550 Fig. 12 shows a Hovmöller diagram of surface geostrophic velocity anomalies in the two re-
551 gions. Visual inspection suggests that eddies in the W09 Box propagate predominantly westward
552 at a relatively coherent phase speed. In the ACC Box, eddies propagate predominantly eastward,
553 though it is less straightforward to identify one particular phase speed directly from the Hovmöller
554 diagram. Instead, eddies seem to propagate at a range of different phase speeds. To quantify the
555 phase speed spectra in the two boxes, we apply the same spectral analysis as for the numerical
556 simulations discussed in section 3. Fig. 13 shows the results of the spectral analysis (analogous in
557 structure to Fig. 7). The predicted phase speeds are plotted on top of the spectra, with the two-layer
558 model parameters chosen as described above.

559 The overall length scales for the ACC Box ($\sim 0.025 - 0.004$ cpkm) are slightly larger than
560 the most energetic scales in our control two-layer QG simulation ($\sim 0.003 - 0.005$ cpkm). This

difference is attributable to the specific choice of parameters in the simulations, though shorter wavelengths may also be under-represented in the AVISO data, due to the spatial smoothing. In the W09 Box, the normalized transverse EKE spectrum (middle panel) shows robust non-dispersive behavior which is consistent with the power spectrum of sea surface elevation shown in Fig. 8 of Wunsch (2009). On the other hand, the raw transverse EKE spectrum (upper panel) shows that the energy-containing eddies mostly fall on the high-wavenumber and -frequency limit of the non-dispersive line identified by Wunsch (2009). The phase speed spectrum (lower panel) for these energy-containing eddies does indicate some systematic variation in the phase speed with eddy scale. In contrast, in the ACC Box, the transverse EKE spectrum exhibits dispersive behavior across a wide range of length scales. This resembles the control case in the reference simulations, which adopts parameters typical of the ACC (compare to Fig. 7)².

Consistent with the results from our two-layer QG simulations, no single dispersion curve completely describes the diagnosed spectrum in either region. Both the raw and normalized transverse EKE power spectra are bounded by the barotropic dispersion curve and reduced gravity curve. It has previously been noted that the vertical structure of ocean eddies is often approximately equivalent barotropic, and lying between the barotropic and reduced gravity limits (e.g. Wunsch 1997; Arbic and Flierl 2004; Wortham 2013; Jansen et al. 2015), and our analysis supports this notion from the perspective of phase speeds.

²We reemphasize that we do not mean to suggest that the true frictional drag in the ACC Box is similar to the relatively large value used in the control reference simulation (i.e. 20 day^{-1}). In the two-layer QG model, frictional strength is a parameter for tuning the strength of the inverse cascade. In fact, in the two-layer QG model, friction is the only parameter that can be modified without affecting the other two non-dimensional parameters. The two-layer QG model lacks many other elements that can influence the inverse cascade and barotropization in the real ocean, such as bottom topography and deep stratification. The net effect of all these factors collectively determines the strength of the inverse cascade and barotropization.

579 In the ACC region, where the two-layer QG model is dynamically appropriate, the reduced grav-
580 ity mode provides the best description of the dispersive wavenumber-frequency energy spectrum.
581 In the subtropics, long waves fall roughly on a non-dispersive line, as documented in Wunsch
582 (2009), but phase speeds of the most energetic mesoscale eddies also exhibit a variation with
583 wavelength suggestive of the influence of barotropic dynamics.

584 Interestingly, the long-wave limit of the reduced gravity mode bisects the peak in the energy
585 spectra in both regions. (For the W09 region, the baroclinic dispersion relation, and its longwave
586 limit, is very similar to the reduced gravity mode, while in the ACC region, the two differ more
587 substantially.) However it remains unclear whether this result is reflective of a fundamental phys-
588 ical process or merely arises from the combined influence of barotropic and baroclinic modes. In
589 both regions the longwave-limit reduced gravity phase speed provides a better estimate at the most
590 energetic scales than the longwave-limit baroclinic phase speed, which has been used in the past
591 to fit eddy phase speeds (e.g. Klocker and Marshall 2014)

592 5. Conclusion

593 Our results demonstrate that, given the degree of barotropization and resulting eddy length scale,
594 linear theory is useful to understanding eddy phase speeds in fully nonlinear two-layer QG baro-
595 clinic turbulence. Analysis of observed sea surface height variability further suggests that the QG
596 model results are also relevant for the interpretation of observed mesoscale eddy phase speeds, at
597 least in selected regions.

598 In the two-layer QG model, eddy phase speeds can be understood largely in terms of the reduced
599 gravity mode and barotropic mode, which represent two relevant limit cases. If the inverse cascade
600 is weak, the phase speed spectrum is reasonably well approximated by the phase speed of the
601 linearly most unstable mode, which in turn can be approximated by the reduced gravity mode

602 dispersion relation. A significant inverse cascade instead leads to barotropization, which in turn
603 leads to phase speeds closer to those of barotropic-mode Rossby waves.

604 Analysis of satellite sea surface height observations suggests that mesoscale eddy phase speeds
605 in the ACC and subtropics are also bounded by these two theoretical dispersion relations. Although
606 two-layer QG dynamics can provide insight into the roles of linear baroclinic and barotropic modes
607 on the eddy phase speed, such a model is clearly overly simplistic, particularly for the subtropical
608 region. This work therefore represents only a step towards better understanding of eddy phase
609 speeds in the real ocean.

610 *Acknowledgments.* Much of this work was carried out at the 2014 Geophysical Fluid Dynam-
611 ics Summer School while L.W. was a visiting student at Woods Hole Oceanographic Institution.
612 M.F.J. and R.P.A acknowledge support from the GFD program. R.P.A acknowledges additional
613 support from NASA award NNX14AI46G. M.F.J. acknowledges additional support from NSF
614 award 1536450. We thank Glenn Flierl, William Young, Rui Xin Huang, and Isaac Held for help-
615 ful comments and discussions.

616 APPENDIX

617 The main advantage of using the zonal spectrum of meridional velocity (i.e. the “transverse”
618 velocity spectrum) is that it better picks up the dominant scales in the two-dimensional total
619 $EKE(k, l)$ spectrum in Fig. 3 (see also Wortham et al. 2014). As shown in Fig. A1, the transverse
620 EKE has vanishing power toward zero zonal wavenumber k , while the total EKE spectrum main-
621 tains high levels at zero k due to contributions from higher meridional wavenumbers. Comparison
622 of Fig. A2 to Fig. 3 suggests that the meridional-mean transverse EKE spectrum exhibits similar
623 peak zonal scales to the two-dimensional total EKE spectrum, whereas the meridional-mean total
624 EKE spectrum exhibits peaks at somewhat smaller wavenumbers and contains significant energy

625 at much smaller wavenumbers. At these small wavenumbers, however, most of the total energy
626 comes from much larger meridional wavenumbers, which makes the interpretation of $\omega - k$ spectra
627 confusing at best.

628 The zonal spectrum of meridional velocity further has the advantage that it is trivially related
629 to the streamfunction variance spectrum, as the factor k^2 can be taken outside of the integral in
630 equation (16). Finally, it is the meridional eddy velocity which is most important for the transport
631 of heat and tracers in the ocean (Klocker and Marshall 2014; Abernathey and Wortham 2015).

632 For the satellite observations, Fig. A3 verifies the largely isotropic behavior of the two selected
633 boxes. As for the QG results, the meridional-mean transverse EKE spectrum captures the peak
634 scales of the two-dimensional total EKE spectrum (Fig. A4, and Fig. A5). We hence adopt trans-
635 verse spectra to interpret eddy phase speeds throughout this paper.

636 **References**

- 637 Abernathey, R., J. Marshall, M. Mazloff, and E. Shuckburgh, 2010: Enhancement of mesoscale
638 eddy stirring at steering levels in the southern ocean. *Journal of Physical Oceanography*, **40** (1),
639 170–184.
- 640 Abernathey, R., C. B. Rocha, F. Poulin, and M. Jansen, 2015: pyqg: v0.1.4. URL <http://dx.doi.org/10.5281/zenodo.32539>, doi:10.5281/zenodo.32539.
- 642 Abernathey, R., and C. Wortham, 2015: Phase speed cross spectra of eddy heat fluxes in the
643 pacific. *Journal of Physical Oceanography*.
- 644 Arbic, B. K., and G. R. Flierl, 2004: Baroclinically unstable geostrophic turbulence in the limits
645 of strong and weak bottom ekman friction: Application to midocean eddies. *Journal of Physical
646 Oceanography*, **34** (10), 2257–2273.
- 647 Bates, M., R. Tulloch, J. Marshall, and R. Ferrari, 2014: Rationalizing the spatial distribution of
648 mesoscale eddy diffusivity in terms of mixing length theory. *Journal of Physical Oceanography*,
649 **44** (6), 1523–1540.
- 650 Chelton, D. B., and M. G. Schlax, 1996: Global observations of oceanic rossby waves. *Science*,
651 **272** (5259), 234–238.
- 652 Chelton, D. B., M. G. Schlax, and R. M. Samelson, 2011: Global observations of nonlinear
653 mesoscale eddies. *Progress in Oceanography*, **91** (2), 167–216.
- 654 Chelton, D. B., M. G. Schlax, R. M. Samelson, and R. A. de Szoeke, 2007: Global observations
655 of large oceanic eddies. *Geophysical Research Letters*, **34** (15), L15 606.
- 656 Cipollini, P., D. Cromwell, P. G. Challenor, and S. Raffaglio, 2001: Rossby waves detected in
657 global ocean colour data. *Geophysical Research Letters*, **28** (2), 323–326.

- 658 Cipollini, P., D. Cromwell, M. S. Jones, G. D. Quartly, and P. G. Challenor, 1997: Concurrent al-
659 timeter and infrared observations of rossby wave propagation near 34°N of the northeast atlantic.
660 *Geophysical Research Letters*, **24** (8), 889–892.
- 661 Dewar, W. K., 1998: On “Too fast” baroclinic planetary waves in the general circulation. *Journal*
662 *of Physical Oceanography*, **28** (9), 1739–1758.
- 663 Early, J. J., R. M. Samelson, and D. B. Chelton, 2011: The evolution and propagation of quasi-
664 geostrophic ocean eddies. *Journal of Physical Oceanography*, **41** (8), 1535–1555.
- 665 Ferrari, R., and M. Nikurashin, 2010: Suppression of eddy diffusivity across jets in the southern
666 ocean. *Journal of Physical Oceanography*, **40** (7), 1501–1519.
- 667 Flierl, G. R., 1978: Models of vertical structure and the calibration of two-layer models. *Dynamics*
668 *of Atmospheres and Oceans*, **2** (4), 341–381.
- 669 Fu, L., 2009: Pattern and velocity of propagation of the global ocean eddy variability. *Journal of*
670 *Geophysical Research: Oceans*, **114** (C11), C11 017.
- 671 Gill, A. E., J. S. A. Green, and A. J. Simmons, 1974: Energy partition in the large-scale ocean
672 circulation and the production of mid-ocean eddies. *Deep Sea Research and Oceanographic*
673 *Abstracts*, **21** (7), 499–528.
- 674 Gouretski, V., and K. Koltermann, 2004: WOCE global hydrographic climatology. *Berichte des*
675 *Bundesamtes für Seeschiffahrt und Hydrographie*, 52.
- 676 Hallberg, R., and A. Gnanadesikan, 2006: The role of eddies in determining the structure and re-
677 sponse of the Wind-Driven southern hemisphere overturning: Results from the modeling eddies
678 in the southern ocean (MESO) project. *Journal of Physical Oceanography*, **36** (12), 2232–2252.

- 679 Hayashi, Y., 1971: A generalized method of resolving disturbances into progressive and retrogressive waves by space fourier and time Cross-Spectral analyses. *Journal of the Meteorological Society of Japan. Ser. II*, **49** (2), 125–128.
- 680
- 681
- 682 Held, I. M., and V. D. Larichev, 1996: A scaling theory for horizontally homogeneous, baroclinically unstable flow on a beta plane. *Journal of the Atmospheric Sciences*, **53** (7), 946–952.
- 683
- 684 Hill, K. L., I. S. Robinson, and P. Cipollini, 2000: Propagation characteristics of extratropical planetary waves observed in the ATSR global sea surface temperature record. *Journal of Geophysical Research: Oceans*, **105** (C9), 21 927–21 945.
- 685
- 686
- 687 Holopainen, E., 1961: On the effect of friction in baroclinic waves. *Tellus*, **13**, 363–367.
- 688
- 689 Holton, J. R., 1992: *An introduction to dynamic meteorology*. 3rd ed., Academic Press, San Diego.
- 690
- Jansen, M. F., A. J. Adcroft, R. Hallberg, and I. M. Held, 2015: Parameterization of eddy fluxes based on a mesoscale energy budget. *Ocean Modelling*, **92**, 28–41.
- 691
- 692 Jansen, M. F., and I. M. Held, 2014: Parameterizing subgrid-scale eddy effects using energetically consistent backscatter. *Ocean Modelling*, **80**, 36–48.
- 693
- 694 Johnson, G. C., and H. L. Bryden, 1989: On the size of the antarctic circumpolar current. *Deep Sea Research Part A. Oceanographic Research Papers*, **36** (1), 39–53.
- 695
- 696 Killworth, P. D., and J. R. Blundell, 2003: Long extratropical planetary wave propagation in the presence of slowly varying mean flow and bottom topography. part i: The local problem. *Journal of Physical Oceanography*, **33** (4), 784–801.
- 697
- 698 Killworth, P. D., and J. R. Blundell, 2004: The dispersion relation for planetary waves in the presence of mean flow and topography. part i: Analytical theory and One-Dimensional examples. *Journal of Physical Oceanography*, **34** (12), 2692–2711.
- 699
- 700

- 701 Killworth, P. D., and J. R. Blundell, 2005: The dispersion relation for planetary waves in the
702 presence of mean flow and topography. part II: Two-Dimensional examples and global results.
703 *Journal of Physical Oceanography*, **35** (11), 2110–2133.
- 704 Killworth, P. D., and J. R. Blundell, 2007: Planetary wave response to surface forcing and insta-
705 bility in the presence of mean flow and topography. *Journal of Physical Oceanography*, **37** (5),
706 1297–1320.
- 707 Killworth, P. D., D. B. Chelton, and R. A. de Szoeke, 1997: The speed of observed and theoretical
708 long extratropical planetary waves. *Journal of Physical Oceanography*, **27** (9), 1946–1966.
- 709 Klocker, A., and R. Abernathey, 2013: Global patterns of mesoscale eddy properties and diffusiv-
710 ities. *Journal of Physical Oceanography*, **44** (3), 1030–1046.
- 711 Klocker, A., R. Ferrari, and J. H. LaCasce, 2012a: Estimating suppression of eddy mixing by
712 mean flows. *Journal of Physical Oceanography*, **42** (9), 1566–1576.
- 713 Klocker, A., R. Ferrari, J. H. Lacasce, and S. T. Merrifield, 2012b: Reconciling float-based and
714 tracer-based estimates of lateral diffusivities. *Journal of Marine Research*, **70** (4), 569–602.
- 715 Klocker, A., and D. P. Marshall, 2014: Advection of baroclinic eddies by depth mean flow. *Geo-
716 physical Research Letters*, **41** (10), 3517–3521.
- 717 Maltrud, M., and G. Vallis, 1991: Energy spectra and coherent structures in forced two-
718 dimensional and beta-plane turbulence. *Journal of Fluid Mechanics*, **228**, 321–342.
- 719 Marshall, J., E. Shuckburgh, H. Jones, and C. Hill, 2006: Estimates and implications of sur-
720 face eddy diffusivity in the southern ocean derived from tracer transport. *Journal of Physical
721 Oceanography*, **36** (9), 1806–1821.

- 722 Mazloff, M. R., P. Heimbach, and C. Wunsch, 2010: An Eddy-Permitting southern ocean state
723 estimate. *Journal of Physical Oceanography*, **40** (5), 880–899.
- 724 McWilliams, J. C., 2006: *Fundamentals of geophysical fluid dynamics*. Cambridge University
725 Press, Cambridge.
- 726 Mcwilliams, J. C., 2008: The nature and consequences of oceanic eddies. *Ocean Modeling in an*
727 *Eddying Regime*, t. W. Hecht, and H. Hasumi, Eds., American Geophysical Union, 5–15.
- 728 McWilliams, J. C., and G. R. Flierl, 1979: On the evolution of isolated, nonlinear vortices. *Journal*
729 *of Physical Oceanography*, **9** (6), 1155–1182.
- 730 Nof, D., 1981: On the β -Induced movement of isolated baroclinic eddies. *Journal of Physical*
731 *Oceanography*, **11** (12), 1662–1672.
- 732 Pedlosky, J., 1979: *Geophysical Fluid Dynamics*. Springer Verlag.
- 733 Randel, W. J., and I. M. Held, 1991: Phase speed spectra of transient eddy fluxes and critical layer
734 absorption. *Journal of the Atmospheric Sciences*, **48** (5), 688–697.
- 735 Rhines, P. B., 1975: Waves and turbulence on a beta-plane. *Journal of Fluid Mechanics*, **69** (03),
736 417–443.
- 737 Rhines, P. B., 1979: Geostrophic turbulence. *Annual Review of Fluid Mechanics*, **11** (1), 401–441.
- 738 Scott, R. B., and F. Wang, 2005: Direct evidence of an oceanic inverse kinetic energy cascade
739 from satellite altimetry. *Journal of Physical Oceanography*, **35** (9), 1650–1666.
- 740 Stammer, D., 1997: Global characteristics of ocean variability estimated from regional
741 TOPEX/POSEIDON altimeter measurements. *Journal of Physical Oceanography*, **27** (8),
742 1743–1769.

- 743 Taylor, G. I., 1938: The spectrum of turbulence. *Proceedings of the Royal Society of London.*
- 744 *Series A - Mathematical and Physical Sciences*, **164 (919)**, 476–490.
- 745 Thompson, A., and W. Young, 2007: Two-layer baroclinic eddy heat fluxes: Zonal flows and
- 746 energy balance. *J. Atmos. Sci.*, **64**, 3214–3231.
- 747 Tulloch, R., J. Marshall, C. Hill, and K. S. Smith, 2011: Scales, growth rates, and spectral fluxes
- 748 of baroclinic instability in the ocean. *Journal of Physical Oceanography*, **41 (6)**, 1057–1076.
- 749 Tulloch, R., J. Marshall, and K. S. Smith, 2009: Interpretation of the propagation of surface
- 750 altimetric observations in terms of planetary waves and geostrophic turbulence. *Journal of Geo-*
- 751 *physical Research: Oceans*, **114 (C2)**, C02 005.
- 752 Vallis, G. K., 2006: *Atmospheric and Oceanic Fluid Dynamics*. Cambridge University Press.
- 753 Waterman, S., N. G. Hogg, and S. R. Jayne, 2011: Eddy–Mean flow interaction in the kuroshio
- 754 extension region. *Journal of Physical Oceanography*, **41 (6)**, 1182–1208.
- 755 Wortham, C., J. Callies, and M. G. Scharffenberg, 2014: Asymmetries between wavenumber
- 756 spectra of along- and Across-Track velocity from tandem mission altimetry. *Journal of Physical*
- 757 *Oceanography*, **44 (4)**, 1151–1160.
- 758 Wortham, C. J. L., 2013: *A multi-dimensional spectral description of ocean variability with ap-*
- 759 *plications*. Massachusetts Institute of Technology and Woods Hole Oceanographic Institution,
- 760 Woods Hole, MA.
- 761 Wunsch, C., 1997: The vertical partition of oceanic horizontal kinetic energy. *Journal of Physical*
- 762 *Oceanography*, **27 (8)**, 1770–1794.
- 763 Wunsch, C., 2009: The oceanic variability spectrum and transport trends. *Atmosphere-Ocean*,
- 764 **47 (4)**, 281–291.

- 765 Wunsch, C., and P. Heimbach, 2007: Practical global oceanic state estimation. *Physica D: Non-*
766 *linear Phenomena*, **230** (1–2), 197–208.
- 767 Zang, X., and C. Wunsch, 1999: The observed dispersion relationship for north pacific rossby
768 wave motions. *Journal of Physical Oceanography*, **29** (9), 2183–2190.

769 LIST OF FIGURES

- Fig. 1.** Linear baroclinic instability calculation for a two-layer QG model with the parameters $\delta = 0.25$ and $\Delta U = 0.04$ m/s. The upper panel shows the growth rate per day of the unstable mode as a function of zonal inverse wavelength normalized by that of the baroclinic radius of deformation $L_d = 15$ km. The lower panel shows the phase speed of these unstable modes. Black, blue, magenta and red curves correspond to no bottom friction case, $(10 \text{ days})^{-1}$ decay rate, $(20 \text{ days})^{-1}$ decay rate and $(40 \text{ days})^{-1}$ decay rate, respectively. Dashed, dash-dot, and dotted curves correspond to the phase speeds of the reduced-gravity mode, barotropic mode, and baroclinic mode, respectively. 42

Fig. 2. Hovmöller diagram of upper layer streamfunction for two-layer QG model as a function of longitude and time. The strong friction experiment (left panel) has bottom friction with $(10 \text{ days})^{-1}$ decay rate, control experiment (middle panel) with $(20 \text{ days})^{-1}$ decay rate, and the weak friction experiment (right panel) with $(40 \text{ days})^{-1}$ decay rate. For each panel, the upper layer streamfunction is normalized with respect to the maximum absolute value within the period to highlight the propagation pattern. 43

Fig. 3. Power spectrum of total EKE ($|(k^2 + l^2)\widehat{\psi_1}^2|/2$) as a function of zonal wavenumber k and meridional wavenumber l for the same three two-layer QG experiments as in Fig. 2. 44

Fig. 4. The same three experiments as shown in Fig. 2. The three solid curves show ratios between barotropic EKE and total EKE of the two layers in nonlinear simulations. The three dashed curves show ratios of barotropic EKE and total EKE in linear unstable modes, with most unstable modes marked as stars. The abscissa is zonal wavenumber normalized by the zonal wavenumber corresponding to the deformation radius. 45

Fig. 5. The solid curves show ratios between barotropic EKE and total EKE from two-layer QG experiments, varying respective non-dimensional parameters, with each overlying dot represents one simulation. The dashed curves show ratios of barotropic EKE to total EKE for the corresponding linearly most unstable modes. The varied non-dimensional parameters are the layer thickness ratio (left), frictional strength (middle), and non-dimensional beta (right). 46

Fig. 6. The top row shows spectral energy budget analysis for the nonlinear two-layer QG simulations as a function of zonal inverse wavelength normalized by radius of deformation as abscissa and the respective non-dimensional parameters as ordinate, i.e. the layer thickness ratio δ (left column), friction strength τ_f^* (second column), and beta β^* (third and fourth columns). The conversion from available potential energy to eddy kinetic energy is shown in blue shading and the barotropic EKE in yellow-to-red contour lines. Both spectral budgets are normalized with respect to their maximum value at each non-dimensional parameter. The contour intervals are identical between the four panels. The bottom shows the linear baroclinic growth rate as a function of zonal inverse wavelength normalized by radius of deformation as abscissa and respective non-dimensional parameters as ordinate. The first contour corresponds to a growth rate of 0.001 per day, and contour intervals are 0.003 per day. 47

Fig. 7. Power spectra (top row) of transverse EKE as a function of frequency and zonal inverse wavelength for the same three two-layer QG experiments as in Fig. 2. The bottom row is the same as the top row, except normalized at each zonal inverse wavelength. Black solid curves are diagnosed eddy phase speeds based on first moments of power spectra. In all panels, Colored thick solid curves are predicted phase speeds with no assumption made regarding its meridional wavenumber l based on Eq. (20), for the baroclinic mode C_{BC} (cyan), reduced-

815	gravity mode C_{RG} (blue) and barotropic mode C_{BT} (green), respectively. For comparison, 816 linear dispersion relations with assumptions of $l = 0$ and $l = k$ are plotted as light solid and 817 dashed curves. The linear unstable modes are presented in white dots with varying marker 818 sizes corresponding to growth rates. The zero phase speed line is highlighted in white. The 819 colored texts in the bottom row indicate the normalized root-mean-square error (%) between 820 predicted and diagnosed eddy phase speeds. See texts for more details.	48
821	Fig. 8. Transverse EKE power spectra (top row) in the nonlinear two-layer QG simulations as a 822 function of zonal phase speed and respective non-dimensional parameters (same order as 823 used in Fig. 6). Dispersion relation curves of the baroclinic mode in long wave limit (cyan), 824 reduced-gravity mode (blue) and barotropic mode (green) are plotted on top of power spec- 825 tra. See text for more details. The bottom row shows the linear growth rate similar as in 826 Fig. 6, but as a function of phase speed in the abscissa. In all panels, the zero phase speed 827 line is highlighted in white.	49
828	Fig. 9. The normalized root-mean-square error (%) of predicted eddy phase speeds (defined follow- 829 ing equation 21) as a function of respective non-dimensional parameters (same order as used 830 in Fig. 6). Each overlying dot represents one simulation. See text for more details.	50
831	Fig. 10. Zonal component of the absolute geostrophic velocity of the AVISO product averaged from 832 year 2012. Two boxes chosen for the analysis are marked.	51
833	Fig. 11. The top row shows zonally-averaged neutral densities (upper left panel) and the correspond- 834 ing first baroclinic mode structure (upper right panel) for the two considered boxes (see 835 legend). The bottom row shows the projection of the full continuous zonally-averaged zonal 836 flow velocity profile for the two boxes onto the barotropic and first baroclinic modes (see 837 text for an explanation of the analog two-layer model.) Note the different ranges in the 838 abscissa between the bottom left and right panels.	52
839	Fig. 12. Hovmöller diagram of meridional geostrophic velocity anomalies from AVISO as a function 840 of longitude and time, at 27.625 N (left) within the W09 Box and 57.625 S (right) within the 841 ACC Box.	53
842	Fig. 13. Similar to Fig. 7, but for the AVISO data during 1993-2004 at the two boxes, the W09 Box 843 (left column) and ACC Box (right column). In addition to the dispersion relations shown 844 in Fig. 7, the dash-dotted blue line here shows the long-wave limit of the reduced gravity 845 mode, and the dashed-dotted cyan line shows the long-wave limit of the baroclinic mode.	54
846	Fig. A1. Power spectrum of transverse EKE ($ k^2 \widehat{\psi}_1^2 /2$) as a function of zonal wavenumber k and 847 meridional wavenumber l for the same three two-layer QG experiments as in Fig. 2.	55
848	Fig. A2. Normalized power spectrum of meridional-mean total EKE ($\int (k^2 + l^2) \widehat{\psi}_1^2 dl / 2$) and 849 meridional-mean transverse EKE ($\int k^2 \widehat{\psi}_1^2 dl / 2$) as a function of zonal wavenumber k for 850 the same three two-layer QG experiments as in Fig. 2.	56
851	Fig. A3. Power spectrum of total EKE ($ (k^2 + l^2) \widehat{\psi}_1^2 /2$) as a function of zonal wavenumber k and 852 meridional wavenumber l for the two selected boxes from AVISO.	57
853	Fig. A4. Power spectrum of transverse EKE ($ k^2 \widehat{\psi}_1^2 /2$) as a function of zonal wavenumber k and 854 meridional wavenumber l for the two selected boxes from AVISO.	58

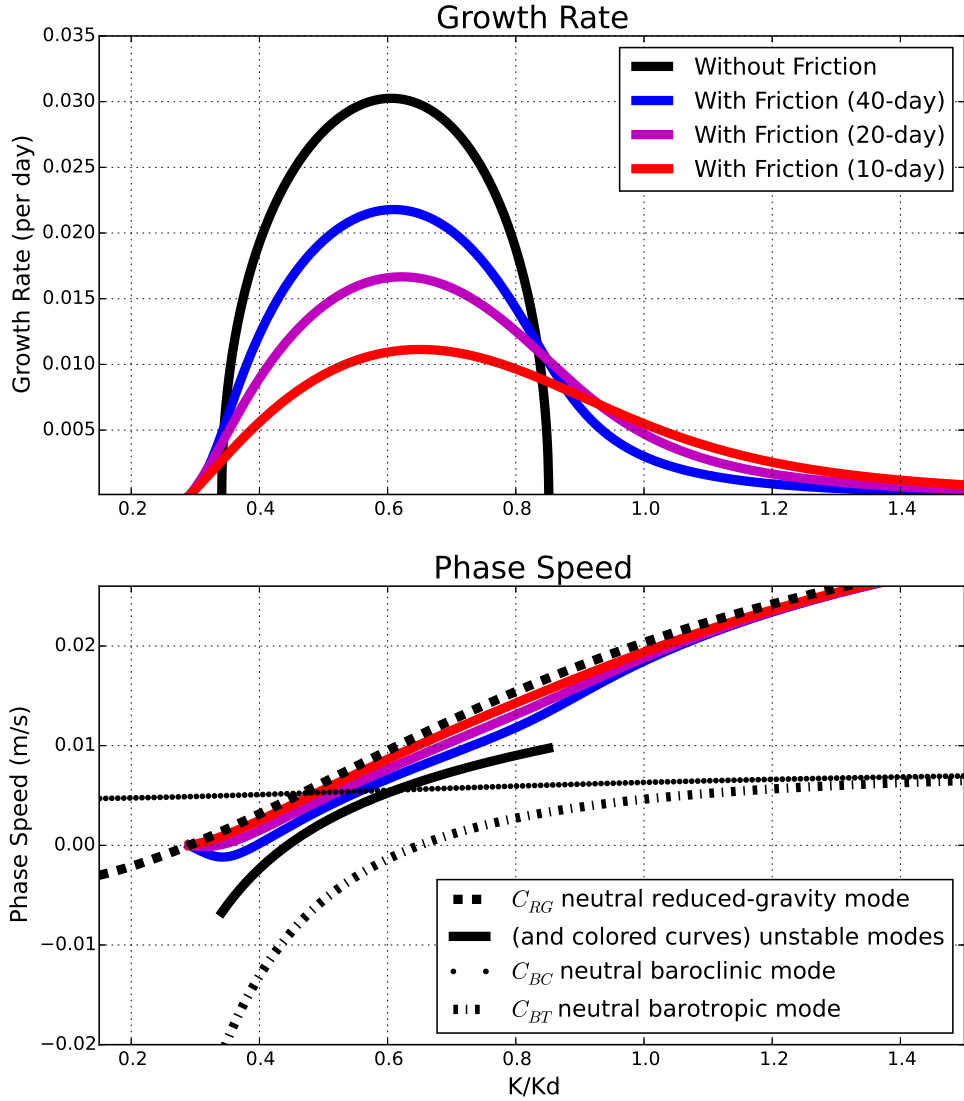
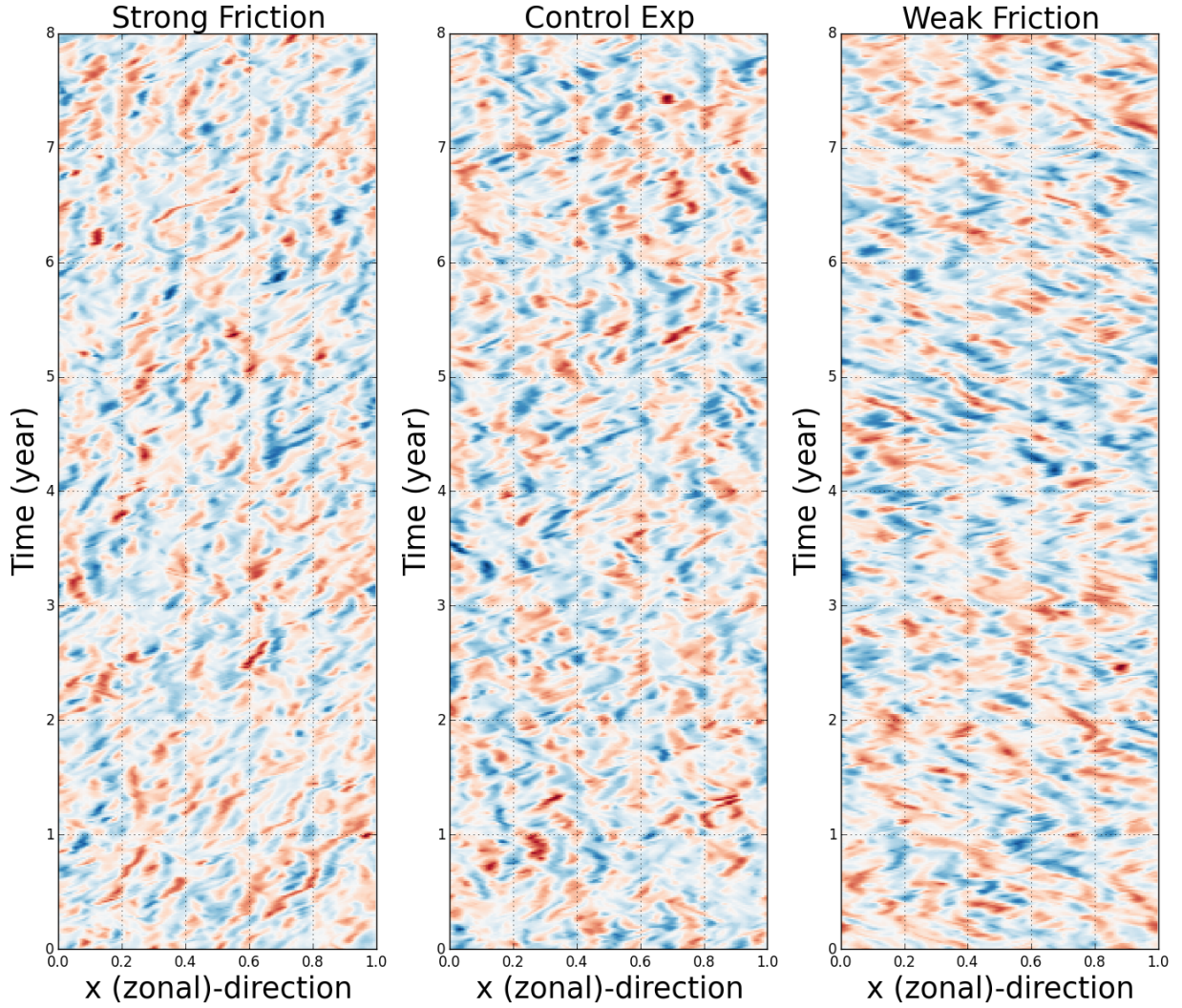


FIG. 1. Linear baroclinic instability calculation for a two-layer QG model with the parameters $\delta = 0.25$ and $\Delta U = 0.04$ m/s. The upper panel shows the growth rate per day of the unstable mode as a function of zonal inverse wavelength normalized by that of the baroclinic radius of deformation $L_d = 15$ km. The lower panel shows the phase speed of these unstable modes. Black, blue, magenta and red curves correspond to no bottom friction case, $(10 \text{ days})^{-1}$ decay rate, $(20 \text{ days})^{-1}$ decay rate and $(40 \text{ days})^{-1}$ decay rate, respectively. Dashed, dash-dot, and dotted curves correspond to the phase speeds of the reduced-gravity mode, barotropic mode, and baroclinic mode, respectively.



865 FIG. 2. Hovmöller diagram of upper layer streamfunction for two-layer QG model as a function of longitude
 866 and time. The strong friction experiment (left panel) has bottom friction with $(10 \text{ days})^{-1}$ decay rate, control
 867 experiment (middle panel) with $(20 \text{ days})^{-1}$ decay rate, and the weak friction experiment (right panel) with $(40$
 868 $\text{days})^{-1}$ decay rate. For each panel, the upper layer streamfunction is normalized with respect to the maximum
 869 absolute value within the period to highlight the propagation pattern.

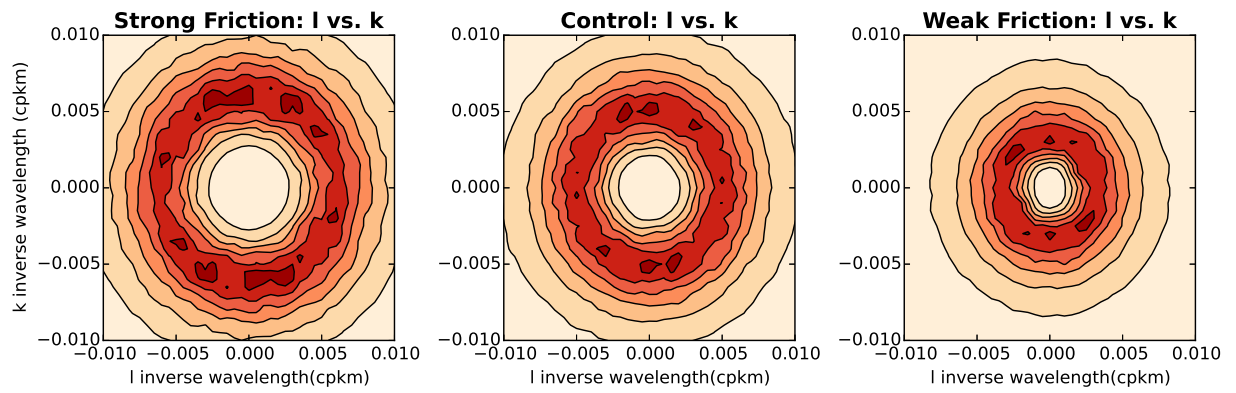
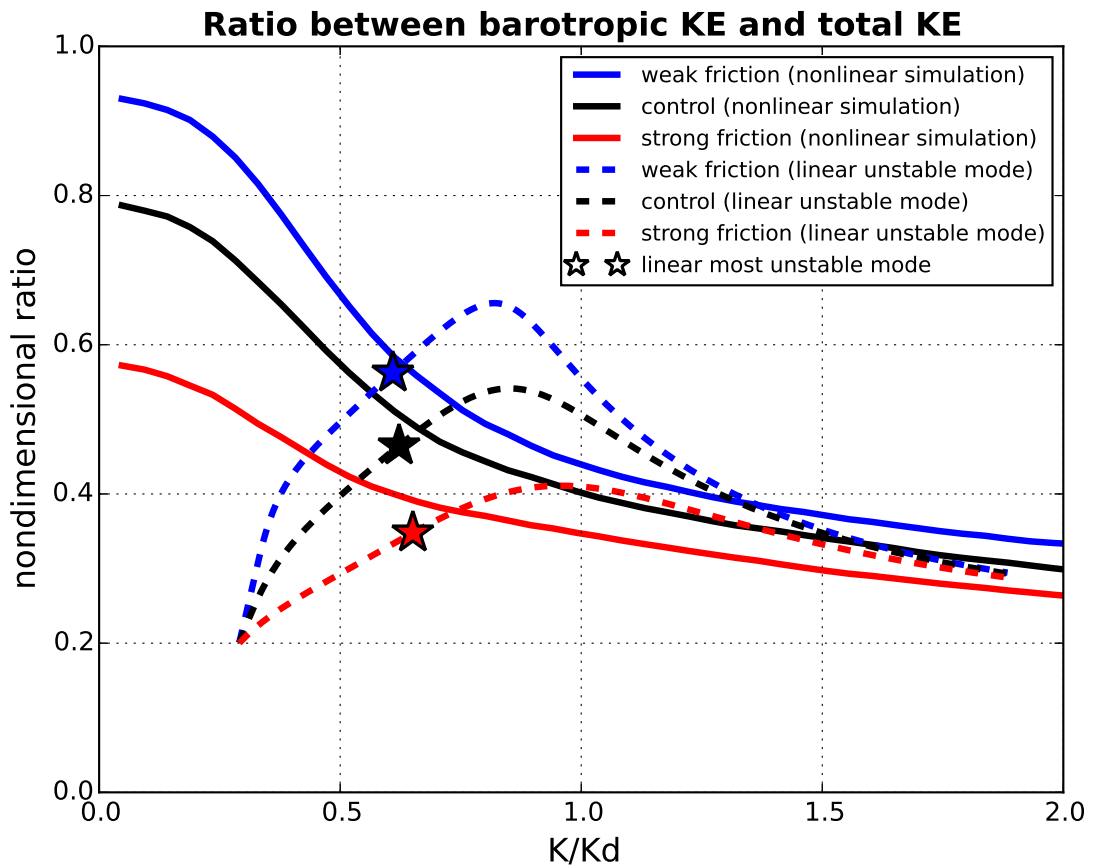
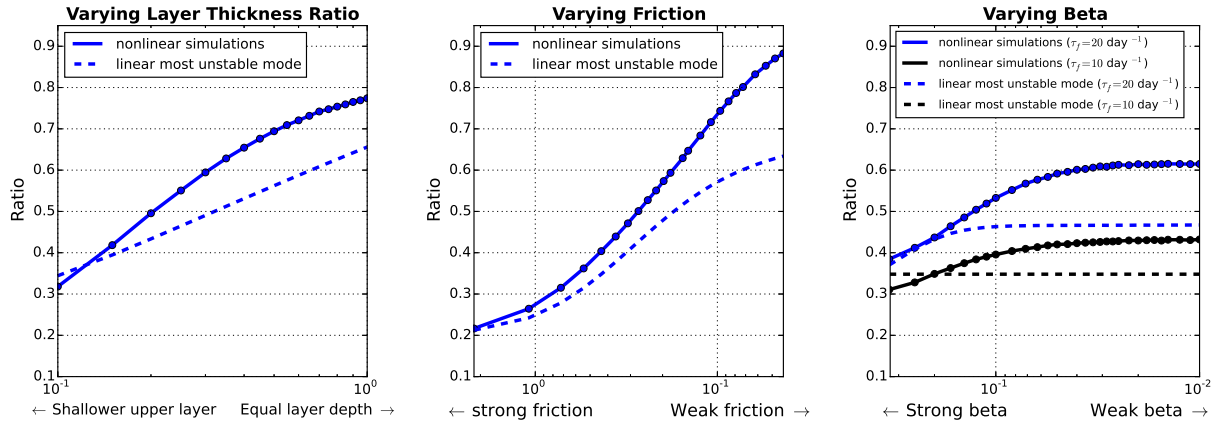


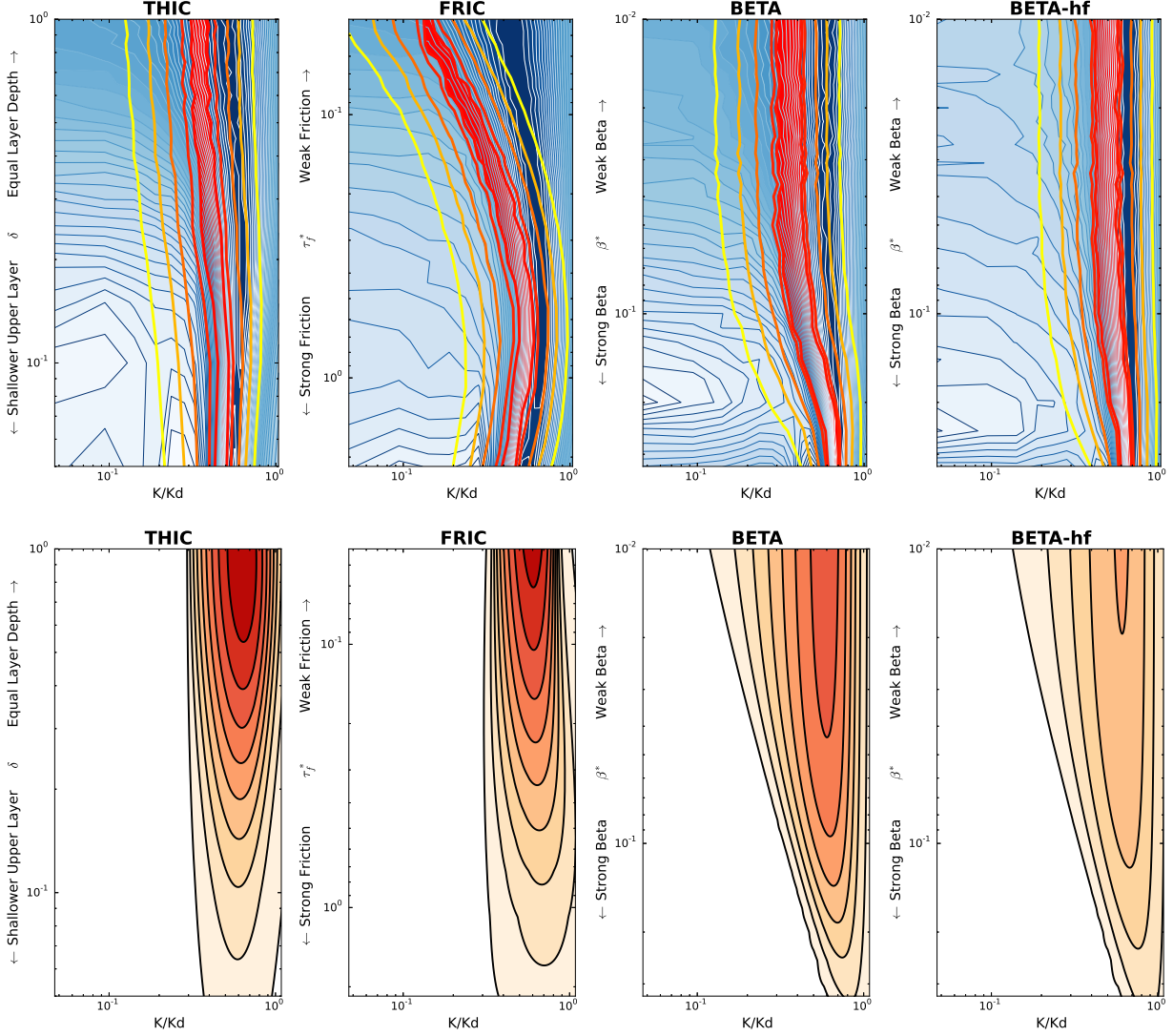
FIG. 3. Power spectrum of total EKE ($|(k^2 + l^2)\widehat{\psi}_1|^2|/2$) as a function of zonal wavenumber k and meridional wavenumber l for the same three two-layer QG experiments as in Fig. 2.



872 FIG. 4. The same three experiments as shown in Fig. 2. The three solid curves show ratios between barotropic
 873 EKE and total EKE of the two layers in nonlinear simulations. The three dashed curves show ratios of barotropic
 874 EKE and total EKE in linear unstable modes, with most unstable modes marked as stars. The abscissa is zonal
 875 wavenumber normalized by the zonal wavenumber corresponding to the deformation radius.



876 FIG. 5. The solid curves show ratios between barotropic EKE and total EKE from two-layer QG experiments,
 877 varying respective non-dimensional parameters, with each overlying dot represents one simulation. The dashed
 878 curves show ratios of barotropic EKE to total EKE for the corresponding linearly most unstable modes. The
 879 varied non-dimensional parameters are the layer thickness ratio (left), frictional strength (middle), and non-
 880 dimensional beta (right).



881 FIG. 6. The top row shows spectral energy budget analysis for the nonlinear two-layer QG simulations as a
 882 function of zonal inverse wavelength normalized by radius of deformation as abscissa and the respective non-
 883 dimensional parameters as ordinate, i.e. the layer thickness ratio δ (left column), friction strength τ_f^* (second
 884 column), and beta β^* (third and fourth columns). The conversion from available potential energy to eddy kinetic
 885 energy is shown in blue shading and the barotropic EKE in yellow-to-red contour lines. Both spectral budgets
 886 are normalized with respect to their maximum value at each non-dimensional parameter. The contour intervals
 887 are identical between the four panels. The bottom shows the linear baroclinic growth rate as a function of zonal
 888 inverse wavelength normalized by radius of deformation as abscissa and respective non-dimensional parameters
 889 as ordinate. The first contour corresponds to a growth rate of 0.001 per day, and contour intervals are 0.003 per
 890 day.

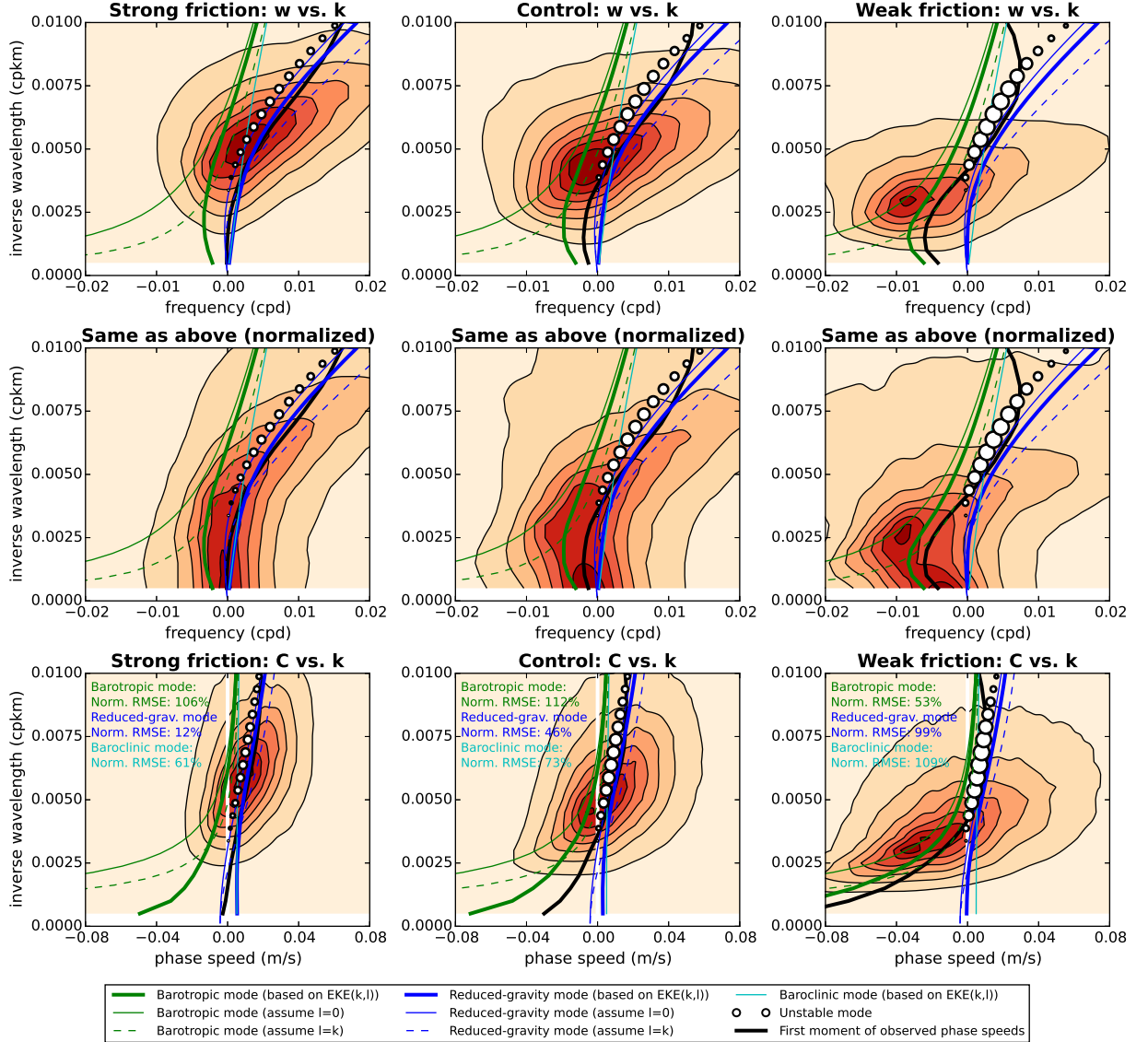
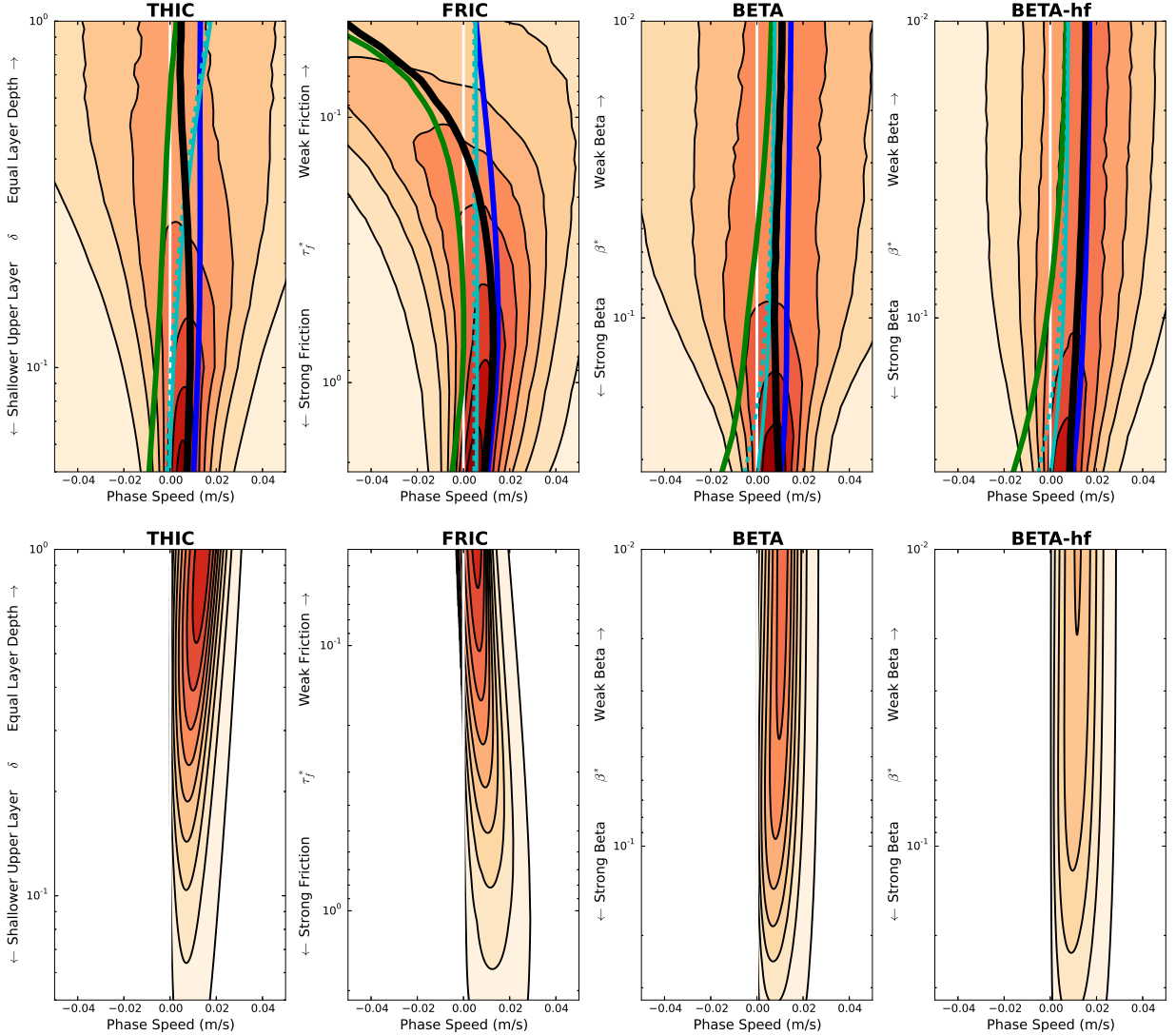
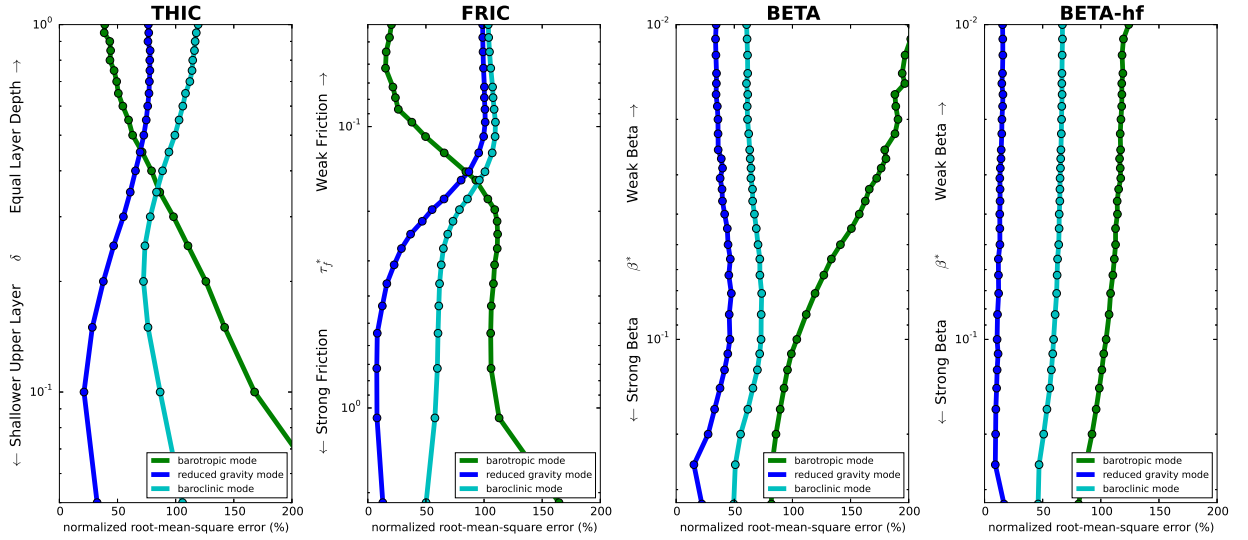


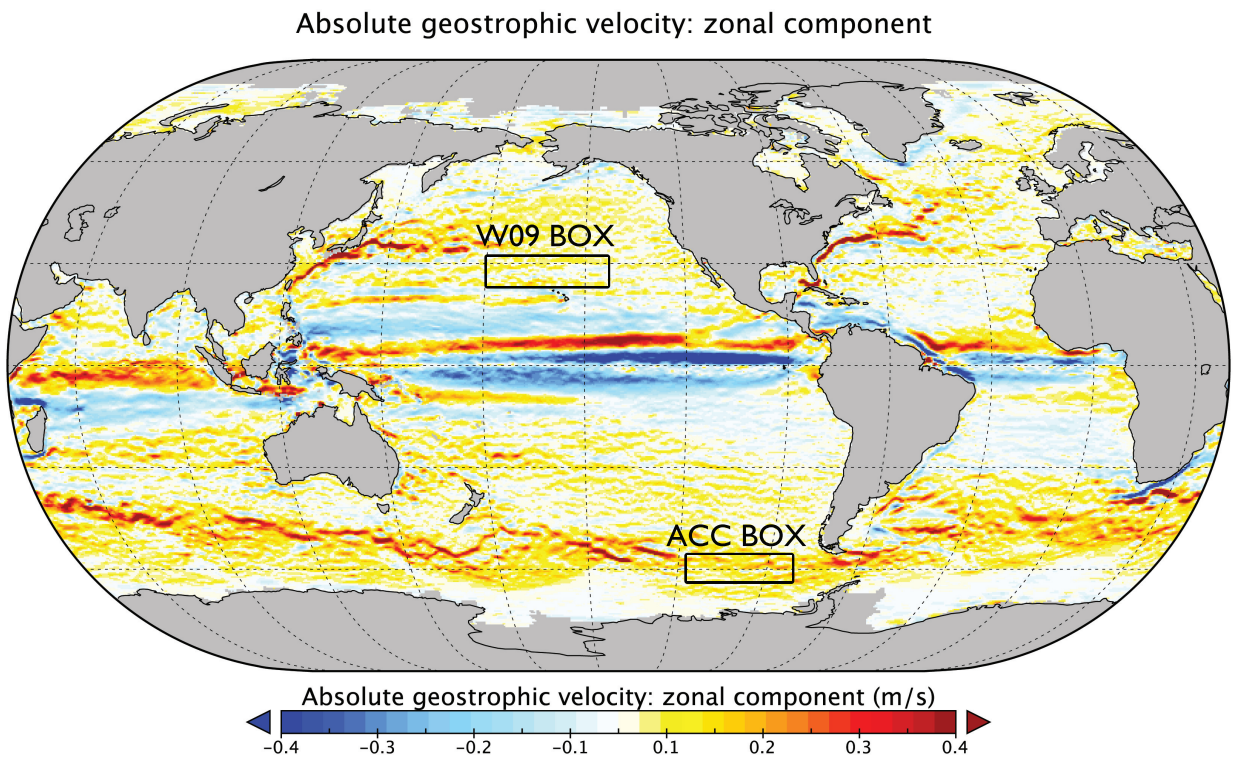
FIG. 7. Power spectra (top row) of transverse EKE as a function of frequency and zonal inverse wavelength for the same three two-layer QG experiments as in Fig. 2. The bottom row is the same as the top row, except normalized at each zonal inverse wavelength. Black solid curves are diagnosed eddy phase speeds based on first moments of power spectra. In all panels, Colored thick solid curves are predicted phase speeds with no assumption made regarding its meridional wavenumber l based on Eq. (20), for the baroclinic mode C_{BC} (cyan), reduced-gravity mode C_{RG} (blue) and barotropic mode C_{BT} (green), respectively. For comparison, linear dispersion relations with assumptions of $l = 0$ and $l = k$ are plotted as light solid and dashed curves. The linear unstable modes are presented in white dots with varying marker sizes corresponding to growth rates. The zero phase speed line is highlighted in white. The colored texts in the bottom row indicate the normalized root-mean-square error (%) between predicted and diagnosed eddy phase speeds. See texts for more details.



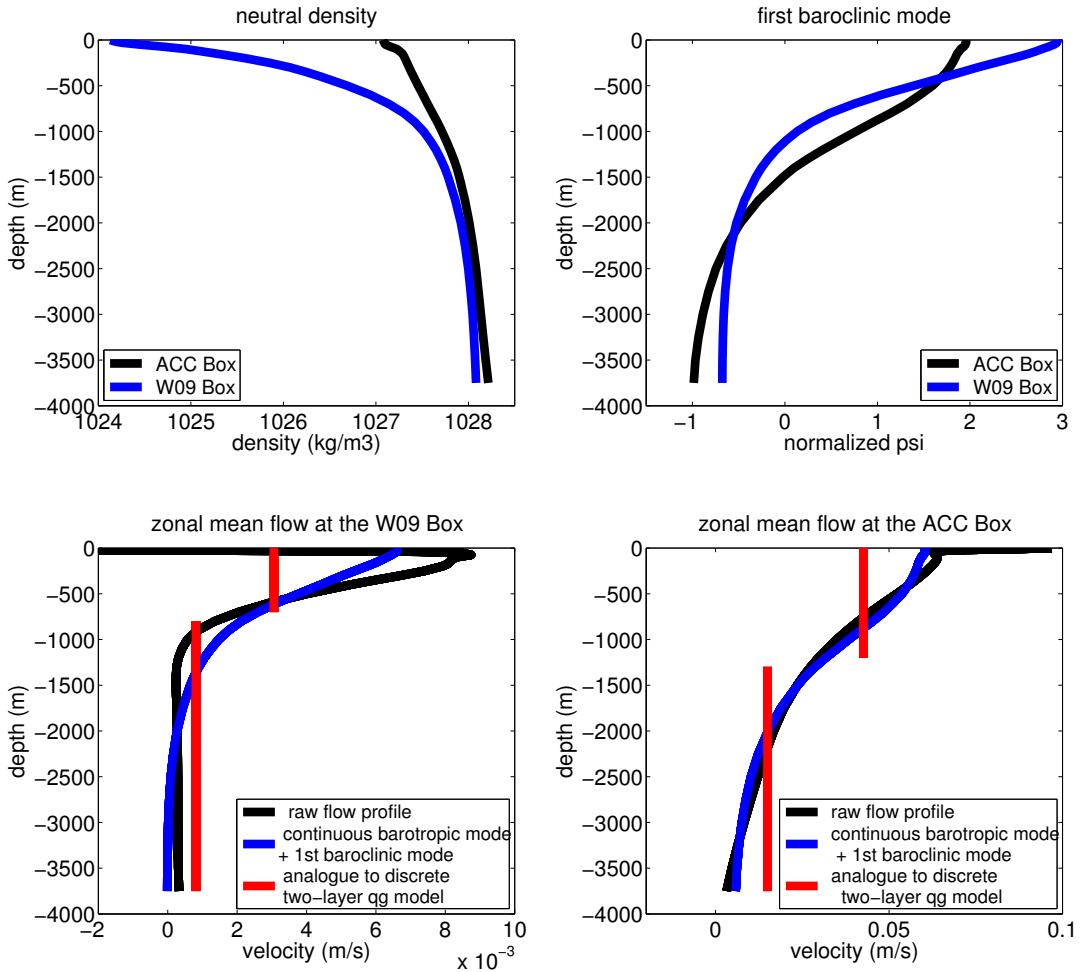
901 FIG. 8. Transverse EKE power spectra (top row) in the nonlinear two-layer QG simulations as a function
902 of zonal phase speed and respective non-dimensional parameters (same order as used in Fig. 6). Dispersion
903 relation curves of the baroclinic mode in long wave limit (cyan), reduced-gravity mode (blue) and barotropic
904 mode (green) are plotted on top of power spectra. See text for more details. The bottom row shows the linear
905 growth rate similar as in Fig. 6, but as a function of phase speed in the abscissa. In all panels, the zero phase
906 speed line is highlighted in white.



907 FIG. 9. The normalized root-mean-square error (%) of predicted eddy phase speeds (defined following equa-
908 tion 21) as a function of respective non-dimensional parameters (same order as used in Fig. 6). Each overlying
909 dot represents one simulation. See text for more details.



910 FIG. 10. Zonal component of the absolute geostrophic velocity of the AVISO product averaged from year
911 2012. Two boxes chosen for the analysis are marked.



912 FIG. 11. The top row shows zonally-averaged neutral densities (upper left panel) and the corresponding first
 913 baroclinic mode structure (upper right panel) for the two considered boxes (see legend). The bottom row shows
 914 the projection of the full continuous zonally-averaged zonal flow velocity profile for the two boxes onto the
 915 barotropic and first baroclinic modes (see text for an explanation of the analog two-layer model.) Note the
 916 different ranges in the abscissa between the bottom left and right panels.

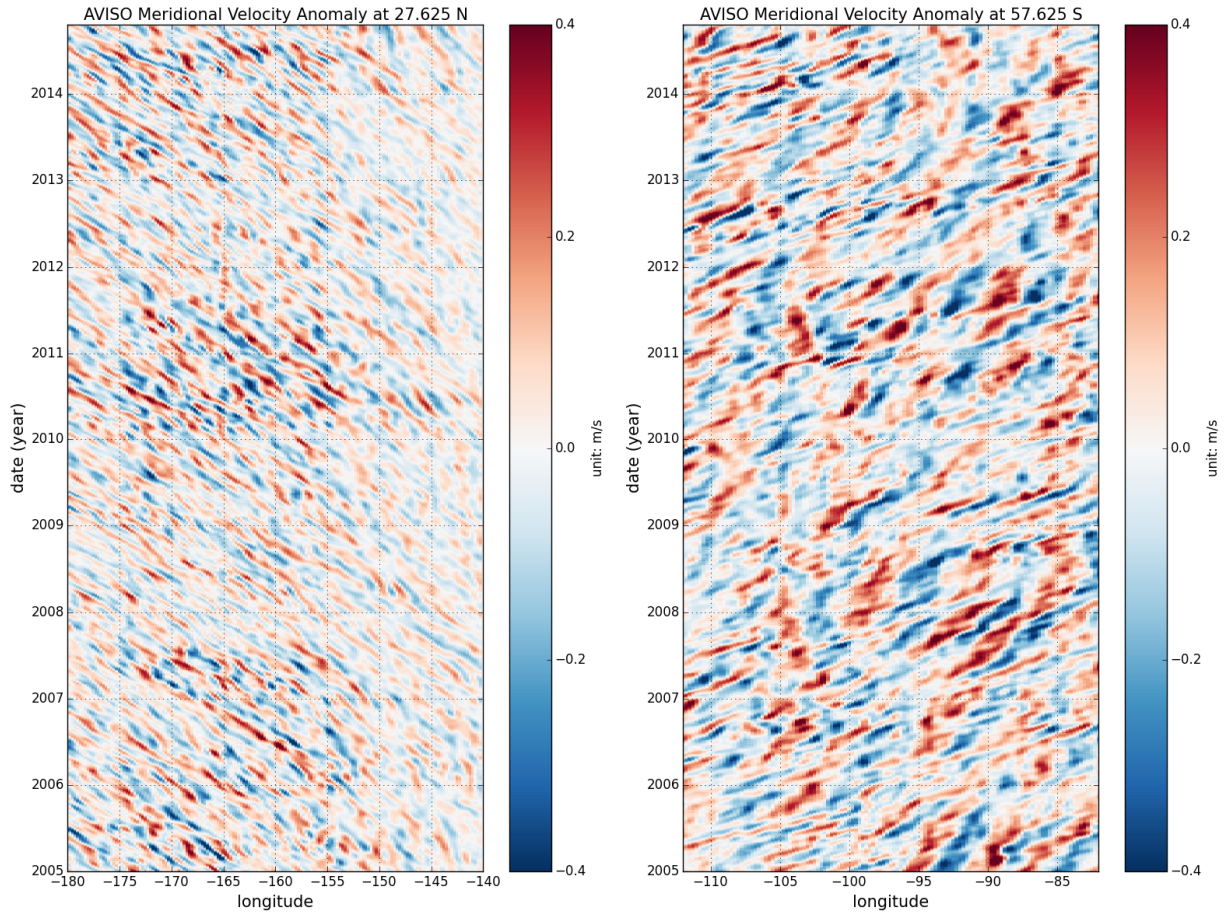


FIG. 12. Hovmöller diagram of meridional geostrophic velocity anomalies from AVISO as a function of longitude and time, at 27.625 N (left) within the W09 Box and 57.625 S (right) within the ACC Box.

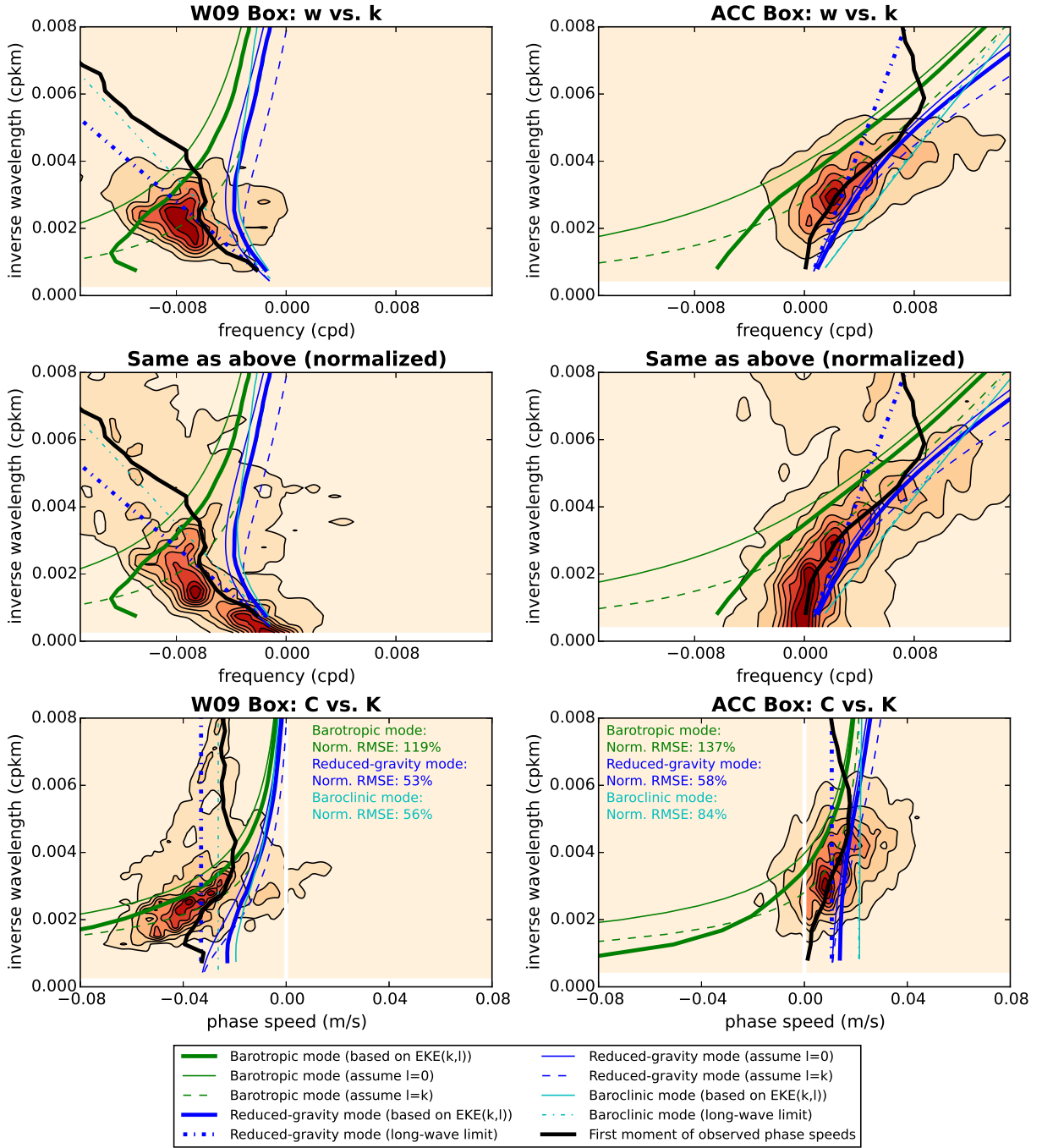
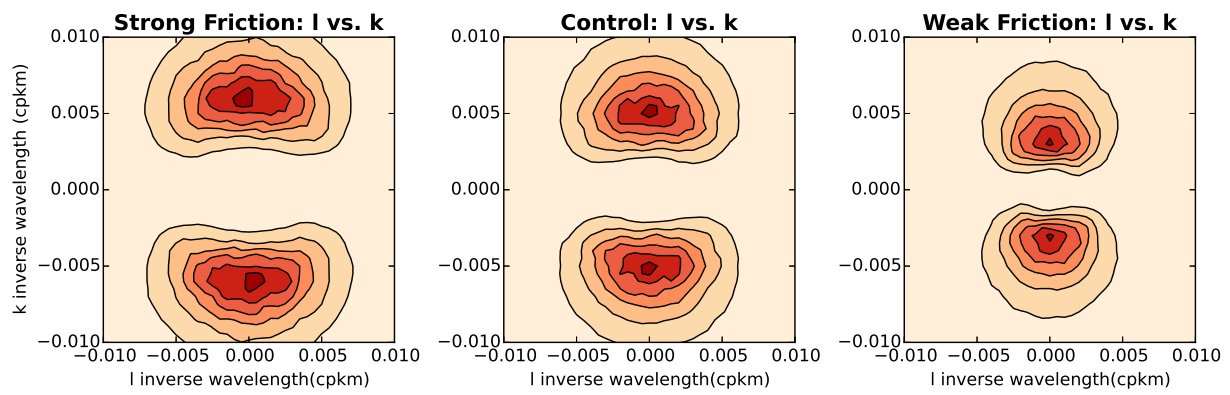
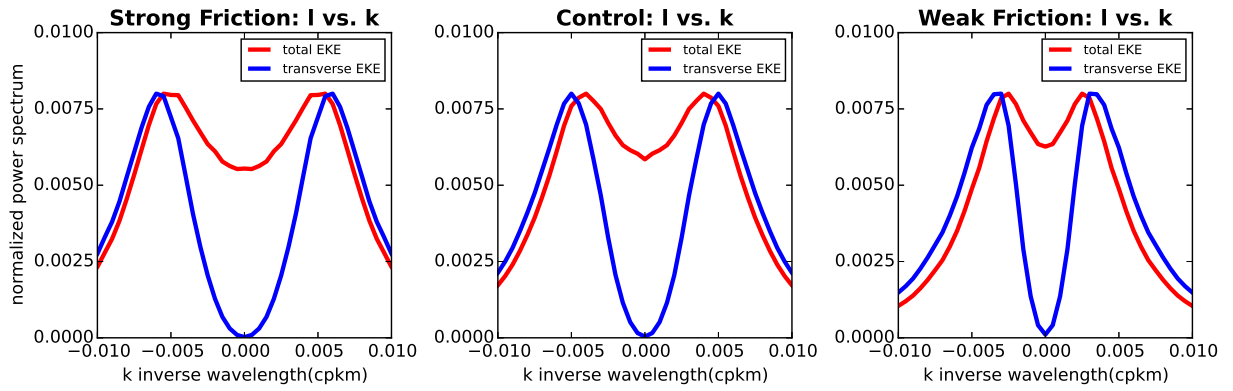


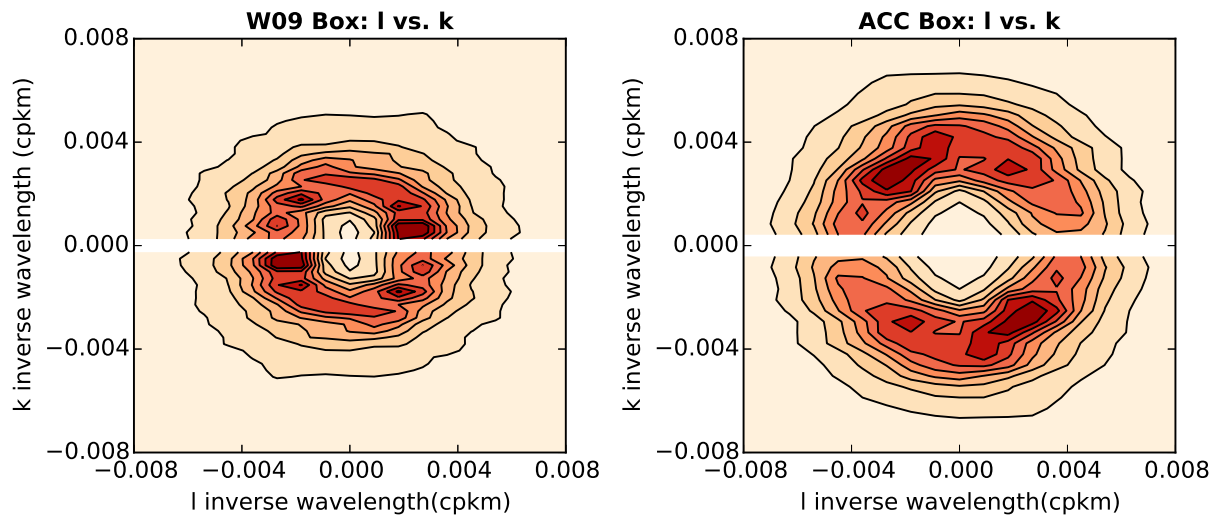
FIG. 13. Similar to Fig. 7, but for the AVISO data during 1993–2004 at the two boxes, the W09 Box (left column) and ACC Box (right column). In addition to the dispersion relations shown in Fig. 7, the dash-dotted blue line here shows the long-wave limit of the reduced gravity mode, and the dashed-dotted cyan line shows the long-wave limit of the baroclinic mode.



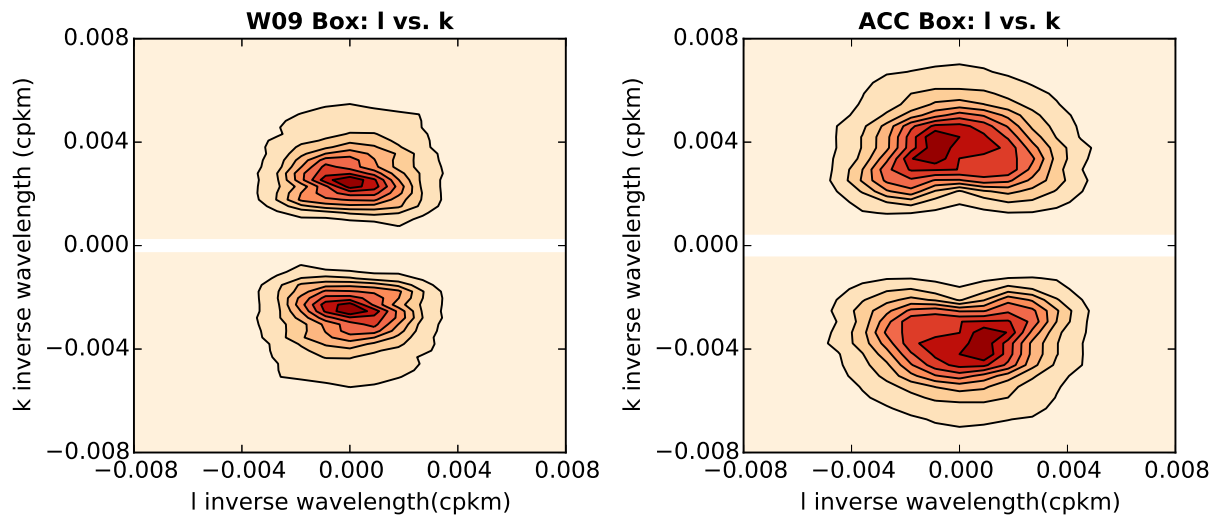
923 Fig. A1. Power spectrum of transverse EKE ($|k^2 \widehat{\psi}_1|^2/2$) as a function of zonal wavenumber k and meridional
 924 wavenumber l for the same three two-layer QG experiments as in Fig. 2.



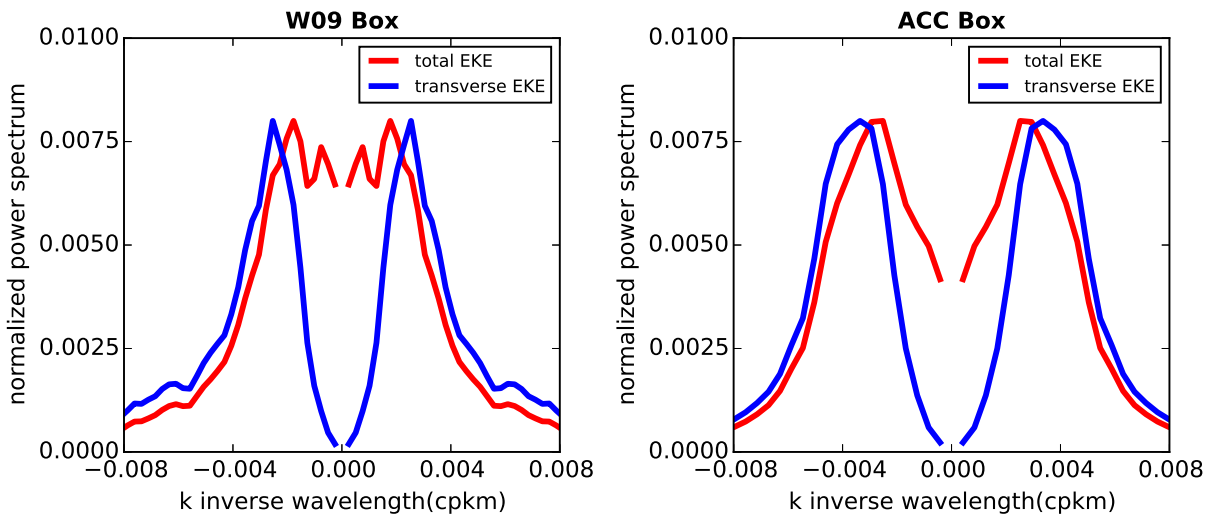
925 Fig. A2. Normalized power spectrum of meridional-mean total EKE ($\int |(k^2 + l^2) \widehat{\psi}_1|^2 dl / 2$) and meridional-
 926 mean transverse EKE ($\int |k^2 \widehat{\psi}_1|^2 dl / 2$) as a function of zonal wavenumber k for the same three two-layer QG
 927 experiments as in Fig. 2.



928 Fig. A3. Power spectrum of total EKE ($|(k^2 + l^2)\widehat{\psi}_1|^2|/2$) as a function of zonal wavenumber k and meridional
 929 wavenumber l for the two selected boxes from AVISO.



930 Fig. A4. Power spectrum of transverse EKE ($|k^2 \widehat{\psi}_1|^2/2$) as a function of zonal wavenumber k and meridional
931 wavenumber l for the two selected boxes from AVISO.



932 Fig. A5. Normalized power spectrum of meridional-mean total EKE ($\int |(k^2 + l^2) \widehat{\psi}_1|^2 dl / 2$) and meridional-
 933 mean transverse EKE ($\int |k^2 \widehat{\psi}_1|^2 dl / 2$) as a function of zonal wavenumber k for the two selected boxes from
 934 AVISO.